# FABRICATION OF $Cu(In,Ga)Se_2$ THIN FILM SOLAR CELLS ON FLEXIBLE METALLIC FOILS

Miss Warittha Thongkham

A Thesis Submitted in Partial Fulfillment of the Requirements
for the Degree of Master of Science Program in Physics
Department of Physics
Faculty of Science
Chulalongkorn University
Academic Year 2011

# การประดิษฐ์เซลล์สุริยะชนิดฟิล์มบางคอปเปอร์อินเดียมแกลเลียมไดซีลิไนด์บนโลหะแผ่นบางชนิดงอได้

นางสาววริษฐา ทองขำ

วิทยานิพนธ์นี้เป็นส่วนหนึ่งของการศึกษาตามหลักสูตรปริญญาวิทยาศาสตรมหาบัณฑิต
สาขาวิชาฟิสิกส์ ภาควิชาฟิสิกส์
คณะวิทยาศาสตร์ จุฬาลงกรณ์มหาวิทยาลัย
ปีการศึกษา 2554

| | |
|---|---|
| Thesis Title | FABRICATION OF Cu(In,Ga)$Se_2$ THIN FILM SOLAR CELLS ON FLEXIBLE METALLIC FOILS |
| By | Miss Warittha Thongkham |
| Field of Study | Physics |
| Thesis Advisor | Assistant Professor Sojiphong Chatraphorn, Ph.D. |

---

Accepted by the Faculty of Science, Chulalongkorn University in Partial Fulfillment of the Requirements for the Master's Degree

……Dean of the Faculty of Science

(Professor Supot Hannongbua, Dr.rer.nat.)

THESIS COMMITTEE

……Chairman

(Assistant Professor Thiti Bovornratanaraks, Ph.D.)

……Thesis Advisor

(Assistant Professor Sojiphong Chatraphorn, Ph.D.)

……Examiner

(Assistant Professor Tonphong Kaewkongka, Ph.D.)

…….External Examiner

(Worawarong Rakreungdet, Ph.D.)

วริษฐา ทองขำ : การประดิษฐ์เซลล์สุริยะชนิดฟิล์มบางคอปเปอร์อินเดียมแกลเลียมไดซีลิไนด์บนโลหะแผ่นบางชนิดงอได้. (FABRICATION OF $Cu(In,Ga)Se_2$ THIN FILM SOLAR CELLS ON METALLIC FOILS) อ.ที่ปรึกษาวิทยานิพนธ์หลัก : ผศ.ดร. โศจิพงศ์ ฉัตราภรณ์, 95 หน้า.

การผลิตเซลล์สุริยะประสิทธิภาพสูงชนิดฟิล์มบางคอปเปอร์อินเดียมแกลเลียมไดซีลิไนด์ (CIGS) บนแผ่นโลหะบางชนิดงอได้ โดยทั่วไปแล้วจำเป็นที่จะต้องมีการปลูกชั้นที่เป็นฉนวนหรือเรียกว่าชั้นที่ขัดขวางการแพร่ของสิ่งเจือปนจำพวกโลหะจากแผ่นรองรับไปยังชั้นดูดกลืนแสง CIGS ในงานนี้ ฟิล์มบาง $Al_2O_3$ ได้ถูกเลือกให้เป็นชั้นที่ขัดขวางการแพร่ เนื่องจากมีความหนาแน่นสูง, มีพันธะแข็งแรง, มีค่าสัมประสิทธิ์การขยายตัวทางความร้อนที่ใกล้เคียงกับแผ่นรองรับสเตนเลส ชนิด 430 และมีความสามารถในการขัดขวางไม่ให้สิ่งเจือปนจำพวกโลหะ อันได้แก่ เหล็ก หรือส่วนประกอบทางเคมีตัวอื่นแพร่จากแผ่นรองรับสเตนเลสไปยังชั้นดูดกลืนแสง CIGS ได้ ซึ่งฟิล์มบาง $Al_2O_3$ จะถูกเคลือบบนแผ่นสเตนเลสบาง ขนาด 3x3 ตารางเซนติเมตร หนา 0.1 มิลลิเมตร ด้วยวิธีอาร์เอฟแมกนิตรอนสปัตเตอริง โดยให้มีความหนาของฟิล์ม $Al_2O_3$ ที่แตกต่างกัน เพื่อจะศึกษาผลของความหนาที่มีต่อประสิทธิภาพของเซลล์ และการเติม Na ก็เป็นอีกปัจจัยหนึ่งที่สำคัญซึ่งส่งผลต่อโครงสร้าง และคุณภาพของชั้นดูดกลืนแสง CIGS โดยผลกระทบของ Na จะถูกศึกษาด้วยวิธีการระเหยร่วม NaF ในกระบวนการปลูกแบบ 3-stage ลักษณะของพื้นผิวและความหนาของฟิล์มสามารถศึกษาได้จาก กล้องจุลทรรศน์แรงอะตอม (AFM) และเปอร์เซ็นต์การสะท้อนของแสง ตามลำดับ โครงสร้างของเซลล์สุริยะประกอบด้วยชั้นฟิล์มบาง ได้แก่ Al/ZnO(Al)/CdS/CIGS/Mo ซึ่งจะถูกเตรียมลงบนชั้น $Al_2O_3$ โดยผลการทดลองจะแสดงถึงความหนาของชั้น $Al_2O_3$ และ ปริมาณ Na ในฟิล์ม CIGS ที่มีอิทธิพลโดยตรงต่อประสิทธิภาพของเซลล์ ซึ่งศึกษาได้จากลักษณะของความหนาแน่นกระแสและความต่างศักย์ (J-V) รวมทั้งผลของประสิทธิภาพของเซลล์ที่ถูกเปรียบเทียบจากการเติม Na โดยใช้วิธีที่แตกต่างกัน

ภาควิชา ฟิสิกส์ ลายมือชื่อนิสิต .....

สาขาวิชา ฟิสิกส์ ลายมือชื่อ อ.ที่ปรึกษาวิทยานิพนธ์หลัก .....

ปีการศึกษา 2554 .....

## 5172438623 : MAJOR PHYSICS

KEYWORDS : $Al_2O_3$ Barrier / Flexible Thin Film Solar Cell / $Cu(In,Ga)Se_2$

WARITTHA THONGKHAM : FABRICATION OF $Cu(In,Ga)Se_2$ THIN FILM SOLAR CELLS ON FLEXIBLE METALLIC FOILS. ADVISOR : ASST. PROF. SOJIPHONG CHATRAPHORN, Ph.D., 95 pp.

The fabrication of high efficiency $Cu(In,Ga)Se_2$ (CIGS) thin film solar cells on flexible metallic foils generally requires the deposition of an insulating or diffusion barrier layer to reduce the diffusion of contaminations from the metallic substrate into the CIGS absorber layer. In this work, the $Al_2O_3$ thin film is chosen as a diffusion barrier, due to its high density, strong ionic bond, coefficient of thermal expansion (CTE) closely matched with the stainless steel (SS type 430) substrate and its ability to block the impurities (Fe and other elements) from the SS into the CIGS absorber. The $Al_2O_3$ thin film is deposited on 3x3 $cm^2$ and 0.1 mm thick SS foils by the RF magnetron sputtering from a pure ceramic target**.** The thicknesses of the $Al_2O_3$ layer are varied in order to study its contribution to the efficiency of the CIGS solar cells. The Na enhancement is one of the most important factors affecting the structure and the quality of the CIGS absorber. The effect of Na is studied by using the NaF co-evaporation in the three-stage deposition process. The morphology and thickness of the films are investigated by atomic force microscopy and optical reflectance spectroscopy, respectively. The solar cells with Al/ZnO(Al)/CdS/CIGS/Mo structure are then fabricated on top of the $Al_2O_3$ layer. The results show that the thicknesses of the $Al_2O_3$ layer and Na content in the CIGS film have a direct influence to the energy conversion efficiency of the solar cells, determined from the current density – voltage (J-V) characteristics of the CIGS solar cells. The methods of Na addition in the CIGS are compared based on the results of the performance of the solar cells.

Department : Physics Student's Signature .....

Field of Study : Physics Advisor's Signature .....

Academic Year : 2011

# Acknowledgments

I would like to express my sincere gratitude to my thesis advisors, Assistant Professor Dr. Sojiphong Chatraphorn and Dr. Chanwit Chityuttakan for their valuable suggestion, scientific skill and advice throughout the work of this thesis.

I would like to thank the committee members, Assistant Professor Dr. Thiti Bovornratanaraks, Assistant Professor Dr. Tonphong Kaewkongka and Dr. Worawarong Rakreungdet for good comments on my thesis.

I would like to thank Semiconductor Physics Research Laboratory (SPRL) and all of SPRL members; Dr. Rachsak Sakdanuphab, Dr. Bancha Athibenjakul, Miss Busarin Noikaew and Miss Boonyaluk Namnuan for their help, kindness guidance and encouragement during the research.

I would like to acknowledge the financial supports from the Thailand Center of Excellence in Physics (ThEP Center).

I would like to thank the Department of Geology, Faculty of Science, Chulalongkorn University for allowing me to access to x-ray diffraction (XRD) facility.

Finally, I would like to thank my parents for encouragement and everything they have done for me throughout the entire study.

# Contents

Page

Page

# List of Tables

Page

Page

# List of Figures

Page

Page

Page

Page

# Chapter I

# Introduction

## 1.1. Overview

To the present day, the research and development of the $Cu(In,Ga)Se_2$ or CIGS thin film solar cells on flexible substrates has attracted many interests for innovative applications such as new building, aeronautic, mobile and space applications [1]. The advantages of using flexible substrate are, for example, they can be applied on curved or uneven surfaces, high flexibility, rolled for storage, low cost, light weight, non-breakability and excellent radiation hardness. There are two main categories of flexible substrates – metallic foils (such as Ti, Mo, Al, stainless steel (SS), etc.) and polymer (polyimide) sheets. A polyimide sheet is one of the candidates for the flexible substrate due to their light weight and has smoother surface than the metallic foils [1]. However, the polyimide sheet is difficult to be heated up to $400^oC$ while high-quality CIGS thin films are grown at high substrate temperature over $500^oC$, and the coefficient of thermal expansion (CTE) is also mismatched with CIGS absorber layer. Table 1.1 shows the values of CTE of substrates and thin film materials used in the fabrication of flexible CIGS thin film solar cells. In this work, the SS foil is chosen as a flexible substrate due to its low cost, high mechanical stability at high temperature during CIGS processing and high conversion efficiency up to 17.5% as achieved by National Renewable Energy Laboratory (NREL), as shown in Table 1.2. On the other hand, the costs of Ti and Mo foils are much more expensive. In general, the requirements for flexible substrate are:

- Film adhesion on substrate; coefficient of thermal expansion (CTE) should match with the absorber layer (CIGS ~ 7-9 x $10^{-6}$/K) in order to prevent the adhesion problem and cracking in each layer during the deposition process,

- High thermal stability; high substrate temperature ($T_{sub}$ > 350$^{o}$C) affects absorber quality and cell performance,

- Vacuum compatibility; the substrate does not outgas during the deposition process in vacuum, especially during CIGS deposition when the substrate is heated,

- Chemical resistance; the substrate does not react with Se during the CIGS deposition process or decompose with CdS solution during the buffer layer deposition process,

- Surface smoothness; roughness surface of substrate (spikes or cavities) leads to shunts between the front and the back contacts and easy for impurity diffusion,

- Cost effectiveness; the flexible substrate is cheap in order to reduce natural resources.

The CIGS thin film solar cells on flexible SS foils typically consist of six different layers of thin film: Al/ ZnO(Al) & i-ZnO/ CdS/ CIGS/ Mo/ diffusion barrier or insulating layer. The insulating layer is additionally introduced into the structure of the solar cells in order to prevent the diffusion of contaminations of Fe and other elements from the SS substrate into the CIGS absorber layer during the CIGS deposition and provide electrical insulation within the cell leading to good quality of devices. The choices of diffusion barrier layer for the flexible solar cells are, for example, $Al_2O_3$, $SiO_{x,}$ etc. In this study, the dielectric $Al_2O_3$ is chosen as the diffusion barrier for the CIGS solar cells on SS foil.

*Table 1.1: Linear coefficients of thermal expansion and maximum substrate temperatures of selected substrate materials, in comparison with CIS [2].*

| Material | CTE ($10^{-6}$ $K^{-1}$) | $T_{s,max}$ (°C) | Notes |
|---|---|---|---|
| SLG | 9 (20–300 °C) | ~600 | Standard glass substrate, contains Na, K, etc. |
| Corning 7059 | 4.6 | >600 | Alkali-free glass |
| Cr steel | 10–11 | >600 | Diffusion of Fe, Ni, Cr, etc.; low-cost substrate |
| Ti | 8.6 | >600 | Low Ti diffusion, restricted Ti purity |
| Ni/Fe-alloys, e.g. Kovar® | 5–11 | >600 | CTE can be well-matched |
| Al | 23–24 | 600 | Low cost, low weight, very high CTE |
| Kapton® E | 17 (20–200 °C) | <500[a] | Polyimide |
| Upilex® S | 12–24 (20–400 °C) | <500[a] | Polyimide |
| ETH-PI | 3 | <500[b] | Polyimide[b] |
| Mo | 4.8–5.9 (20–600 °C) | >600 | Back contact |
| $CuInSe_2$ | 11.2–11.4/7.9–8.6 (20 °C) | | $\perp c$-axis/$\parallel c$-axis |
| ZnO | 4.75/2.9 | | $\perp c$-axis/$\parallel c$-axis |
| $SiO_x$ | 1–9 | >600 | Insulation layer and/or diffusion barrier |
| $Al_2O_3$ | 6–8 | >600 | Insulation layer and/or diffusion barrier |

*Table 1.2: Efficiencies of small area chalcopyrite-based solar cells on flexible substrates from different laboratories [3]*

Selected AM1.5 efficiencies ($\eta$) of small-area chalcopyrite-based solar cells on flexible substrates from different laboratories

| Laboratory[a] | Substrate[b] | Material/technology | $\eta^c$ (%) (AM 1.5) | Reference |
|---|---|---|---|---|
| NREL | SS | CIGS (coevaporation) | 17.5 | Tuttle et al. (2000) |
| Matsushita | SS | CIGS (coevap.) | 17.0 (act. area) | Hashimoto et al. (2003) |
| DayStar Technol. (USA)/NREL | "Metal" | CIGS (coevap.) | 16.9 | Tuttle et al. (2000) |
| Hahn-Meitner-Institut (GER) | Ti | CIGS (coevap.) | 16.2 | Kaufmann et al. (2004) |
| ZSW/Univ. Stuttgart (GER) | Ferritic steel ($Al_2O_3$ barrier) | CIGS (coevap.) | 13.8 | Kessler et al. (2001) |
| ZSW/Univ. Stuttgart (GER) | Ti ($SiO_x$/$SiO_x$:Na barriers) | CIGS (coevap.) | 13.1 | Herrmann et al. (2003) |
| Matsushita | SS ($SiO_2$ barrier) | CIGS (coevap.); Na-free | 12.3 | Satoh et al. (2003) |
| GSE/ITN | SS | CIGS (coevap.) | 11.7 | Wiedeman et al. (2002) |
| ISET | Mo | CIGS (oxide particle precursors, selenization) | 11.7 | Kapur et al. (2003) |
| Florida Solar Energy Center (USA) | SS | Cu(In,Ga)$S_2$ (sputtered precursors, sulphurization) | 10.4 | Dhere et al. (2002) |
| Inst. für Solar Technol. (GER) | Cu tape | $CuInS_2$ (sulphurization) | 9.1 | Tober et al. (2003) |
| CIS Solartechnik GmbH (GER) | Cu or SS (with barriers) | CIGS (ED of precursors, RTP) | 9.0 | Kampmann et al. (2003) |
| ETH (SWI) | PI (lift-off) | CIGS (coevap.) | 12.8 | Tiwari et al. (1999) |
| IEC, Univ. Delaware (USA) | PI | CIGS (coevap.); Na-free | 11.5 (12.1% AR) | Hanket et al. (2002) |
| GSE/ITN | PI | CIGS (coevap.); Na-free | 11.3 | Wiedeman et al. (2002) |
| ZSW/Univ. Stuttgart | PI | CIGS (coevap.) | 10.6 | Kessler et al. (2001) |
| ISET | PI (Upilex) | CIGS (oxide particle precursors, selenization) | 8.9 | Kapur et al. (2003) |
| Solarion GmbH (GER) | Polymer | CIGS (ion beam assisted co-evap.) | 8 | Solarion (2003) |

[a] NREL = National Renewable Energy Laboratory (USA); Matsushita = Matsushita Electric Industrial Co. (JAP); GSE = Global Solar Energy (USA); ITN = ITN Energy Systems (USA); ISET = International Solar Electric Technology Inc. (USA).
[b] SS = stainless steel; PI = polyimide.
[c] Act. area = active area; AR = with anti-reflection coating.

*Table 1.3: Typical chemical composition of the soda-lime glass substrate [4]*

| **Compound** | $SiO_2$ | $Na_2O$ | CaO | MgO | $K_2O$ | $Al_2O_3$ | $SO_3$ | $Fe_2O_3$ |
|---|---|---|---|---|---|---|---|---|
| **Content** | 72.2% | 14.3% | 6.4% | 4.3% | 1.2% | 1.2% | 0.3% | 0.03% |

In addition, the performances of CIGS solar cells on a standard substrate or soda-lime glass (SLG) indicate that the efficiency is higher than that on the metallic substrates due to the influence of Na or alkali doping release from the SLG substrate into the p-type CIGS layer. The chemical composition of SLG is shown in Table 1.3. Na incorporation in the flexible solar cell can help improving the cell efficiency by using NaF compound as external Na source in this thesis.

## 1.2. Objectives of the thesis

1) To obtain suitable fabrication conditions of $Cu(In,Ga)Se_2$ or CIGS thin film solar cells on flexible metallic foils.

2) To study the formation of thin films on flexible substrates at low and high substrate temperature during the absorber processing and influence of substrate temperature that affects the quality of CIGS thin film and devices.

3) To study the performances of flexible CIGS thin film solar cells at different $Al_2O_3$ thicknesses.

4) To study the influence and steps of Na incorporation or alkali doping to the cell performances.

## 1.3. Thesis Outline

This thesis has altogether of five chapters. In the following chapters, chapter 2 describes theoretical background and the principle of the CIGS solar cell and thin film deposition techniques. The experimental procedures; sample preparation, the fabrication details and material properties of standard CIGS thin film solar cells on SLG substrates and the characterization techniques are given in chapter 3. In chapter 4, the experimental details on flexible CIGS thin film solar cells and results are described. Chapter 5 is the summary remarks of thesis.

# Chapter II

# Theoretical Background

This chapter briefly describes the material properties of Cu(In,Ga)$Se_2$, the principle of p-n junction, electrical properties of solar cells, thin film deposition techniques (i.e., molecular beam deposition (MBD) and sputtering technique) and the coefficient of thermal expansion (CTE) that is one of the important factors to the selection of materials for the fabrication of flexible solar cell.

## 2.1. Basic concept of CIGS thin film solar cell

### 2.1.1. CIGS material properties

The efficiency of solar cells depends on the types of material used as a light absorber layer, for example, Si, GaAs, Cu(In,Ga)$Se_2$, CdTe, etc. In this work, Cu(In,Ga)$Se_2$ is chosen as absorber material due to its highest optical absorption as shown in Fig. 2.1 for its absorption coefficient (α) versus energy band gap compared with several other absorber materials used for the solar cell fabrication.

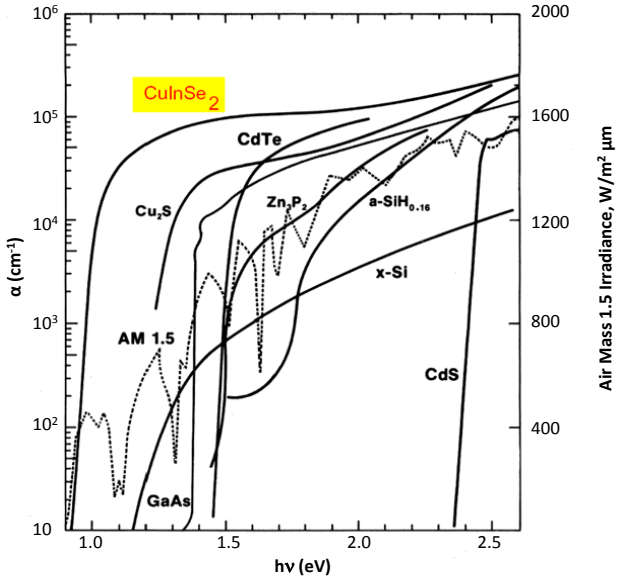


*Figure 2.1: Absorption spectra of $CuInSe_2$ and other absorbers [5].*

CIGS is a direct band gap semiconductor with the highest absorption coefficient of about $10^5$ $cm^{-1}$ when compared with the other semiconductor materials. Its energy band gap ($E_g$) is in the range of 1.04-1.68 eV when alloyed with Ga. The energy band gap variation for the CIGS is given by [6]

$$E_{g,CIGS}(x) = (1-x)E_{g,CIS} + xE_{g,CGS} - bx(1-x), \qquad (2.1)$$

where $x$ is the $\frac{[Ga]}{[Ga]+[In]}$ ratio in the CIGS and $b$ is the bowing parameter (0.15-0.24 eV).

The addition of Ga atoms in the CIGS structure directly affects the open circuit voltage ($V_{oc}$) of the CIGS solar cell by the shifting of the conduction band ($E_c$) and the built-in potential level ($V_{bi}$) up. The range of the band gap energy for the highest efficiency of CIGS thin film solar cells is in the range 1.1-1.5 eV as shown in Fig. 2.2.

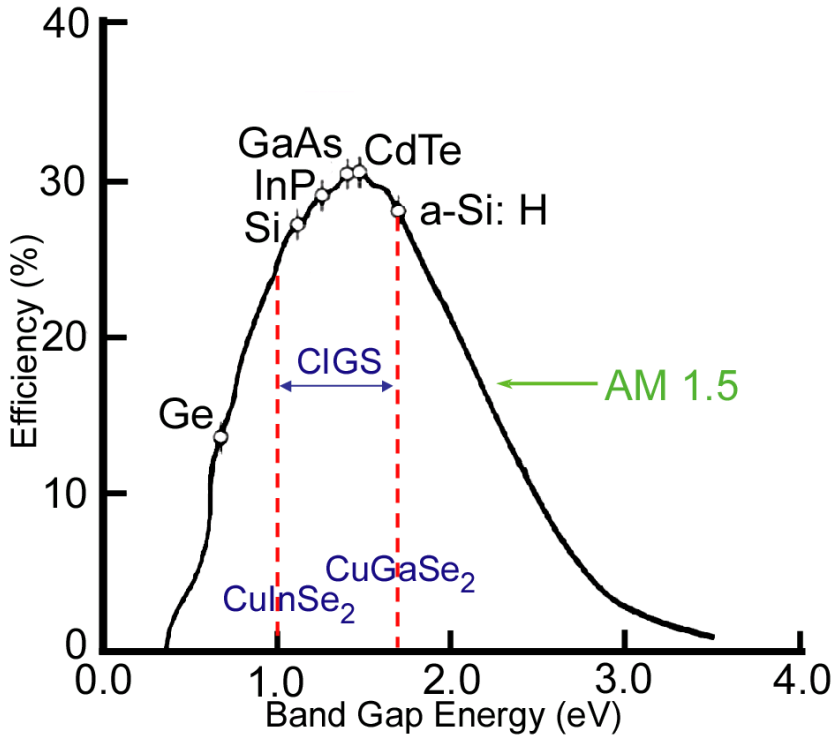


*Figure 2.2: Theoretical cell efficiency of CIGS solar cell and other absorber materials as a function of energy band gap at AM 1.5 [7].*

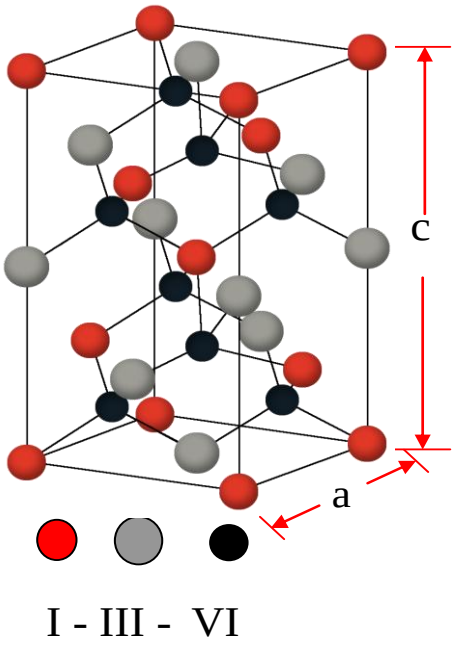


*Figure 2.3: The chalcopyrite structure of CIGS (red atoms are Cu, gray atoms are In or Ga and black atoms are Se) [8].*

The crystal structure of CIGS material is the chalcopyrite structure or α phase (space group $I\bar{4}2d$ ) that consists of a double-stacked zincblende structure as shown in Fig. 2.3. Each metal atom (Cu and In/Ga) is surrounded by four Se atoms as the nearest neighbors. Each Se atom is enclosed with tetrahedral bonded by two Cu atoms and two In/Ga atoms. The typical values of lattice constants (*a* and *c*) of CIGS is shown in Table 2.1.

*Table 2.1: The lattice parameters a and c of CIGS with different x values [9]*

| ***x* ratio** | **Lattice parameters** | |
|---|---|---|
| | ***a* (Å)** | ***c* (Å)** |
| 0.10 | 5.763 | 11.578 |
| 0.20 | 5.744 | 11.514 |
| 0.30 | 5.726 | 11.451 |
| 0.40 | 5.707 | 11.387 |

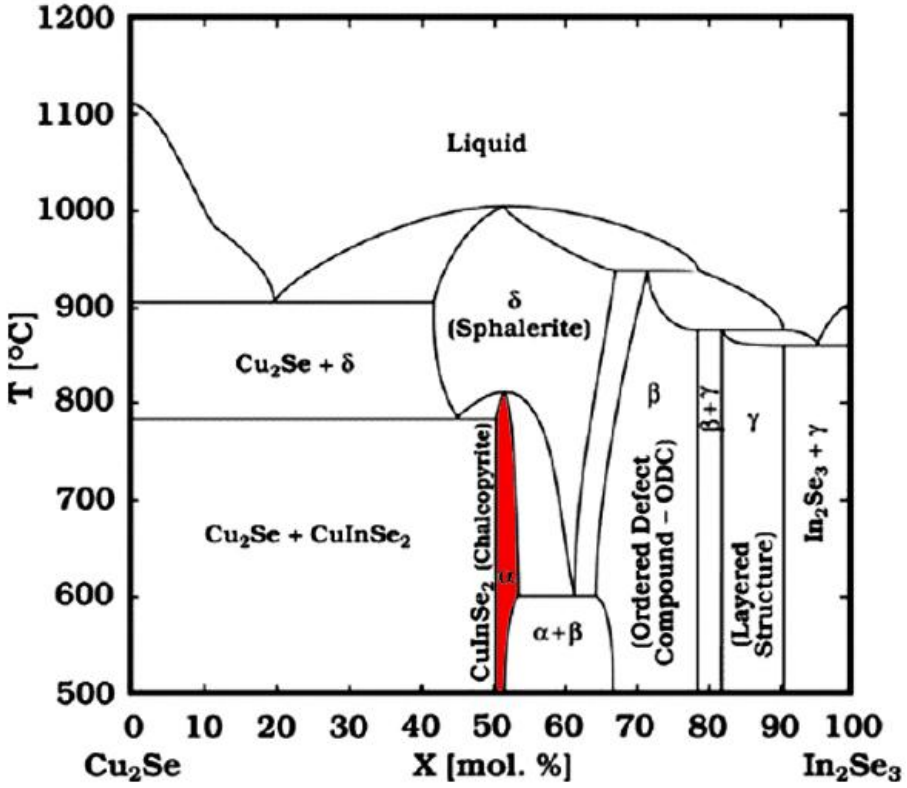


*Figure 2.4: Phase diagram of the $Cu_2Se$ and $In_2Se_3$ for $CuInSe_2$ or CIS material [10].*

Note that, the α phase occurs when the *y* ratio $\left(\frac{[Cu]}{[Ga]+[In]}\right)$ is between 0.9 and 1.0 or slightly Cu deficient that corresponds to *x* value of approximately 50-53 mol.% from the CIS phase diagram shown in Fig. 2.4 for the temperature below 600$^{o}$C.

### 2.1.2. Heterojunction in the CIGS thin film solar cell

The heterojunction is a junction formation between two different semiconductors. In this work, the p-type CIGS absorber and n-type ZnO window/CdS buffer have been chosen for a p-n junction of the devices. The energy band diagram for CIGS thin film solar cell is shown in Fig. 2.5. In the dark (no illumination), electrons (majority carriers) are diffused from the n region to the p region due to the difference of electron (n-type) and hole (p-type) concentration. The interface area of ZnO/CdS layers is the positive side while the CIGS is the negative side leading to the creation of the depletion or space charge region and the electrical built-in potential or

internal electric field at the junction. The main processes of the conversion in the CIGS solar cell can be summarized by the following steps:

(i) Absorption of the photon energy ( $\geq E_g$ of the CIGS ); When the solar cell is illuminated on the ZnO window side, photons with energy equal to or greater than the band energy gap ($E_g$) of the CIGS are absorbed. The photon absorption of the semiconductor materials can simply be described by

$$I = I_0 e^{-\alpha(\lambda)d}, \qquad (2.2)$$

where $I_0$ is the intensity of incident light, $\alpha(\lambda)$ is the absorption coefficient which is the function of wavelength and $d$ is the thickness of material.

(ii) Generation of electron-hole pairs (or carriers); Electrons are excited to the conduction band ($E_c$) of the CIGS and leaving holes in the valence band ($E_v$). This process is known as the generation of electron-hole pairs.

(iii) Diffusion and separation of minority carriers at the depletion region; Electrons (from p-type side) and holes (from n-type side) are diffused to the depletion region and are separated by the influence of the internal electric field. Electrons are transported to the n region and holes to the p region.

(iv) Collection of carriers at the front/back contacts (Al-grid/Mo); The minority carriers are collected by the metallic contact and this generates the photocurrent when it is connected to the external circuit.

In addition, the electron-hole recombination can also occur due to the defect states within the CIGS layer or the interface defects at the heterojunction. The band diagram of the p-n junction between the CIGS and the CdS layers is schematically shown in Fig. 2.5. There is a small spike ($\Delta E_c > 0$) in the conduction band at the CIGS and CdS interface. The spike helps decreasing the interface recombination and increase the built-in potential leading to the increase of photocurrent and open circuit voltage, respectively.

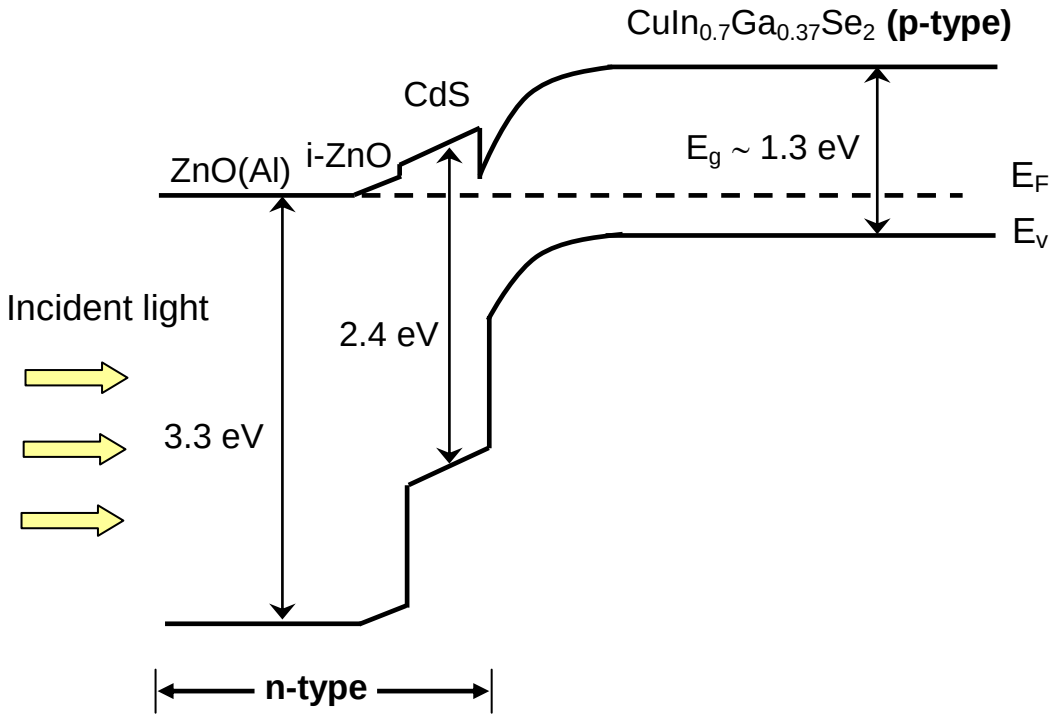


*Figure 2.5: Energy band diagram of p-n heterojunction of CIGS thin film solar cell.*

## 2.2. J-V characteristics of the solar cells

The performance of the CIGS solar cell can be investigated through the current density-voltage (J-V) characteristic in the dark mode and under AM1.5 illumination or light mode. The solar cell has four important key parameters; the short-circuit current density ($J_{sc}$), the open-circuit voltage ($V_{oc}$), the fill factor ($FF$) and the energy conversion efficiency ($\eta$).

In the dark mode, the solar cell is an ideal diode that can be described by the Shockley diode equation [11]

$$J_{dark}(V) = J_0(e^{qV/k_BT} - 1), \qquad (2.3)$$

where $J_{dark}$ is the dark current density, $J_0$ is the saturation current density (constant), $q$ is the electronic charge, $V$ is the applied bias voltage, $k_B$ is the Boltzmann constant and $T$ is the temperature of the solar cell in Kelvin. This mode uses the bias voltage in the drive of the current flow.

In the light mode, the solar cell is illuminated ($V$=0). The current is generated from the absorption of incident light known as the photocurrent ($J_L$) or the short-circuit current ($J_{sc}$) that has an opposite direction of flow with the dark current ($J_{dark}$). Therefore, the sum of current density in the solar cell is

$$J(V) = J_{sc} - J_{dark}(V) = J_{sc} - J_0(e^{qV/k_BT} - 1), \qquad (2.4)$$

Figure 2.6 (a) shows the equivalent circuit of a solar cell that consists of two resistances. The series resistance ($R_s$) is the resistance of films in the CIGS solar cell that depends on the electrical property of materials. The parallel or shunt resistance ($R_{sh}$) has a direct effect to the current flow at the p-n heterojunction region and depends on the leak path or tunneling path from internal imperfections of the films. The leakage current of solar cell increases with the decreasing of the shunt resistance. In the ideal case, $R_s$ is zero and $R_{sh}$ is infinite. When these resistances are included, the equation becomes

$$J = J_{sc} - J_0(e^{q(V+JR_s)/kT} - 1) - \frac{V + JR_s}{R_{sh}}. \qquad (2.5)$$

The open-circuit voltage ($V_{oc}$) is obtained by setting $J$=0, $R_s \to 0$ and $R_{sh} \to \infty$ in Eq. (2.5), and can be written as

$$V_{oc} = \frac{kT}{q}\ln(\frac{J_{sc}}{J_0} + 1). \qquad (2.6)$$

It can be seen from Eq. (2.6) that $V_{oc}$ depends on (i) the intensity of incident light; the value of $J_{sc}$ increases with light intensity and (ii) the properties of semiconductor material, especially the CIGS absorber layer, that affect to the $J_0$ value.

The fill factor ($FF$) can be described with the rectangular area in the $J$-$V$ curve which is defined as

$$FF = \frac{J_m V_m}{J_{sc} V_{oc}}, \qquad (2.7)$$

where $J_m$ and $V_m$ are the maximum of current density and voltage leading to the maximum output power density ($P_m$=$J_m V_m$), respectively. For a good p-n heterojunction of high efficiency solar cell, the FF values are in the range of 0.7-0.85.

The solar cell efficiency ($\eta$) is the ratio of the maximum output power density to the incident light power density ($P_i$);

$$\eta = \frac{J_m V_m}{P_i}, \tag{2.8}$$

The relationship between $\eta$ and $FF$ from Eq. (2.7) is

$$\eta = \frac{J_{sc} V_{oc} FF}{P_i}. \tag{2.9}$$

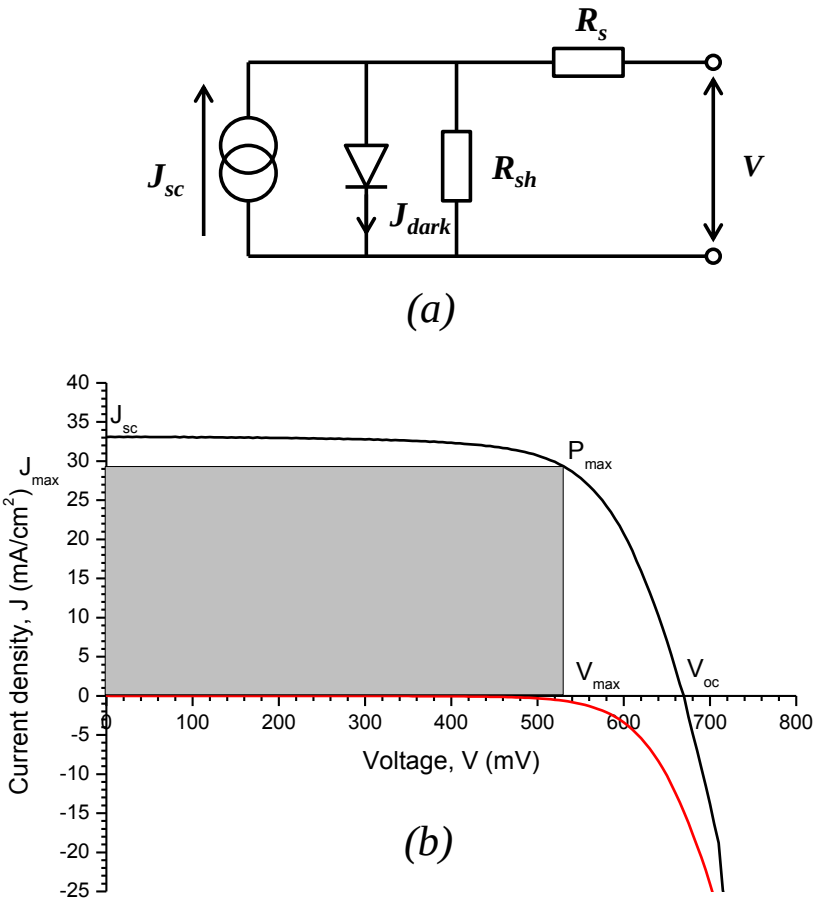


*Figure 2.6: (a) Equivalent circuit of solar cell for the one diode model and (b) J-V characteristic of standard solar cell on soda-lime glass substrate.*

## 2.3. Thin film deposition techniques

The physical vapor deposition (PVD) is the technique used to transfer atoms from the solid or molten source onto the substrate and to create the film formation without the chemical reaction. In this work, the thermal evaporation and the magnetron sputtering techniques which are important methods for the thin film deposition of flexible CIGS solar cell are chosen. The basic details of these methods are briefly described as the followings.

### 2.3.1. Molecular beam deposition (MBD)

The molecular beam deposition is the thermal co-evaporation technique employing the ultrahigh vacuum system (~$10^{-9}$-$10^{-10}$ Torr) to obtain the high quality films due to its very clean environment and a large mean free path. The MBD is a suitable technique for the CIGS growth with high reproducibility. The MBD system consists of the growth chamber and pumping system as schematically shown in Fig. 2.7 (a).

In the growth chamber, there are several evaporation sources known as the Knudsen effusion cells (K-cells) used for the evaporation of Cu, In, Ga and Se. The range of the source temperatures used in the MBD system depends on the vapor pressure of the materials. The relationship between vapor pressure ($P$) and temperature ($T$) of each element can be calculated by the Clausius-Clapyeron equation

$$\frac{dP}{dT} = \frac{P\Delta H(T)}{RT^2}, \tag{2.10}$$

where $\Delta H(T)$ is the changes of enthalpy by $\Delta H(T) = \Delta H_e$ , $\Delta H_e$ is the molar heat of evaporation (constant) and $R$ is the gas constant.

Integration of Eq. (2.10) yields

$$\ln P \approx -\frac{\Delta H_e}{RT} + I, \tag{2.11}$$

or

$$P = Ae^{-\frac{\Delta H_e}{RT}}, \tag{2.12}$$

where $I$ (or $A = e^{I}$ ) is the constant from the integration. The example of relationship between vapor pressure vs. temperature of various materials is shown in Fig. 2.8.

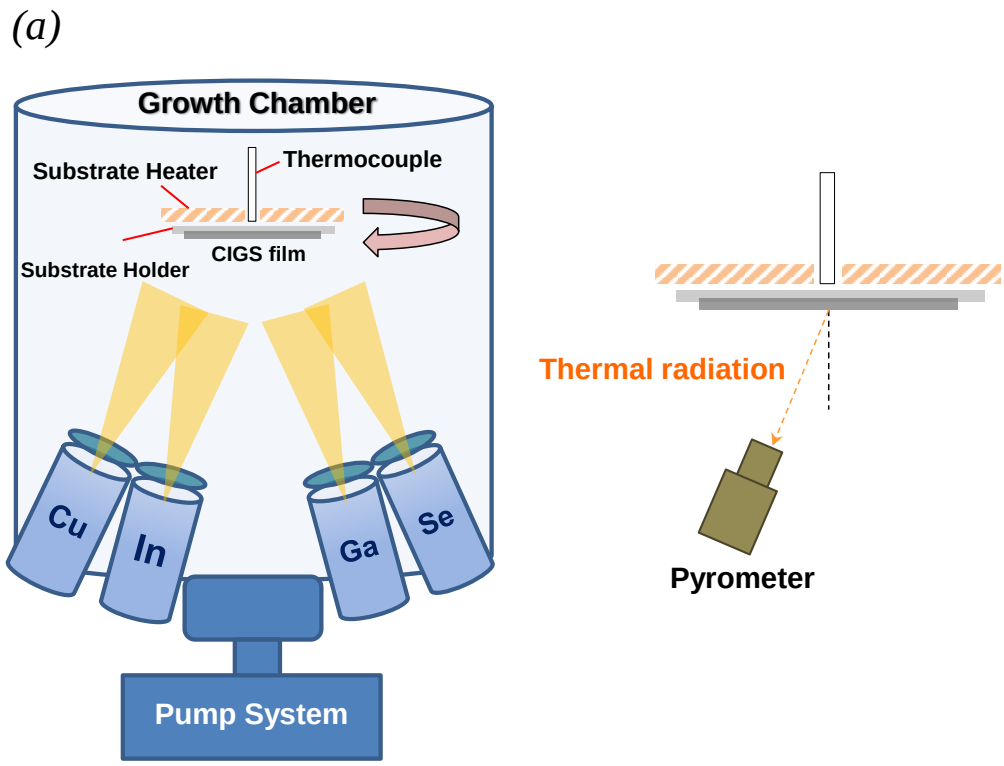


*Figure 2.7: (a) Schematic of the MBD system and (b) Photograph of EW100 MBE system at SPRL*

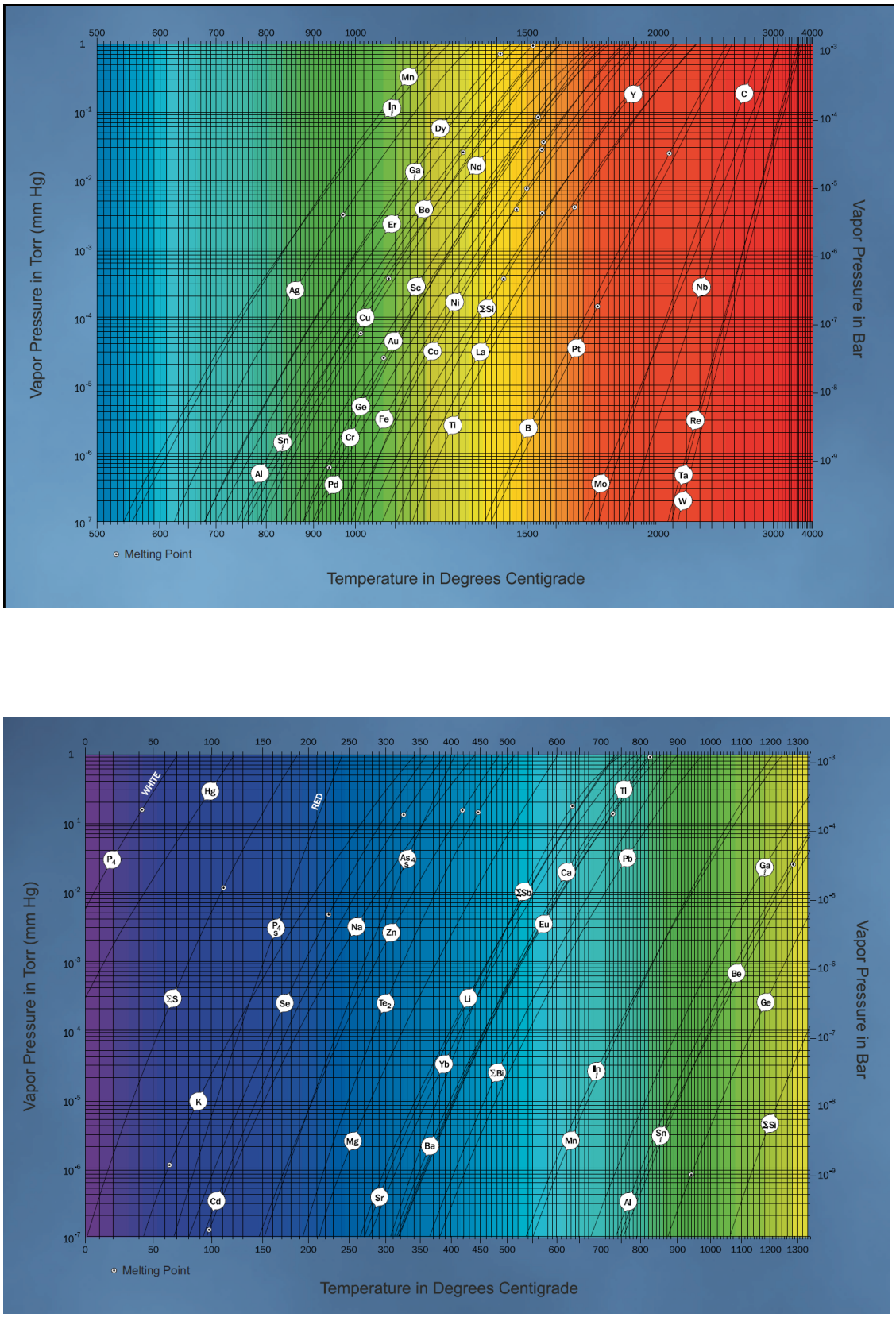


*Figure 2.8: Vapor pressure versus temperature of several materials. Dots correspond to melting points [12].*

One of the important components for the MBD system is the pyrometer which is used to measure thermal radiation from the substrate surface (i.e. Mo/$Al_2O_3$/SS or Mo/SS) and to detect the evolution of the CIGS composition during the deposition process. The substrate is typically heated by a tantalum heater. The principle of the pyrometer can be described by Stefan-Boltzmann law given by

$$j^* = \varepsilon\sigma T^4, \tag{2.13}$$

where $j^*$ is the intensity of thermal radiation from substrate surface, $\varepsilon$ is the emissivity of material, $\sigma$ is the Stefan-Boltzmann constant and $T$ is the surface temperature. For this work, $\varepsilon$ value is set at 0.11 for the Mo surface.

### 2.3.2. Sputtering technique

The magnetron sputtering system can be depicted by Fig. 2.9 (a). The vacuum chamber consists of a substrate holder and targets on the sputtering guns for direct current (DC) and radio frequency (RF) modes. The DC sputtering known as diode or cathodic sputtering is typically used to deposit metals or conducting thin films while the RF sputtering is typically used for oxide or insulating thin films. The advantage of the magnetron sputtering is the high deposition rate and the reduction of electron bombardment on the substrate due to the magnetic field lines prolong and confinement of the electron in the plasma that increases the probability of ion collisions on the target from the electron ionization process of sputtering gas (Ar) as shown in Fig. 2.9 (b). The reaction is

$$Ar + e^- \rightarrow Ar^+ + 2e^-, \tag{2.14}$$

where neutral Ar atom is ionized by primary electron, yielding $Ar^+$ and two electrons. These electrons can ionize more Ar atoms and lead to the glow discharge mechanism.

The deposition rate and quality of films depend on the sputtering gas pressure in the growth chamber that affects the mean free path and power used in the sputtering.

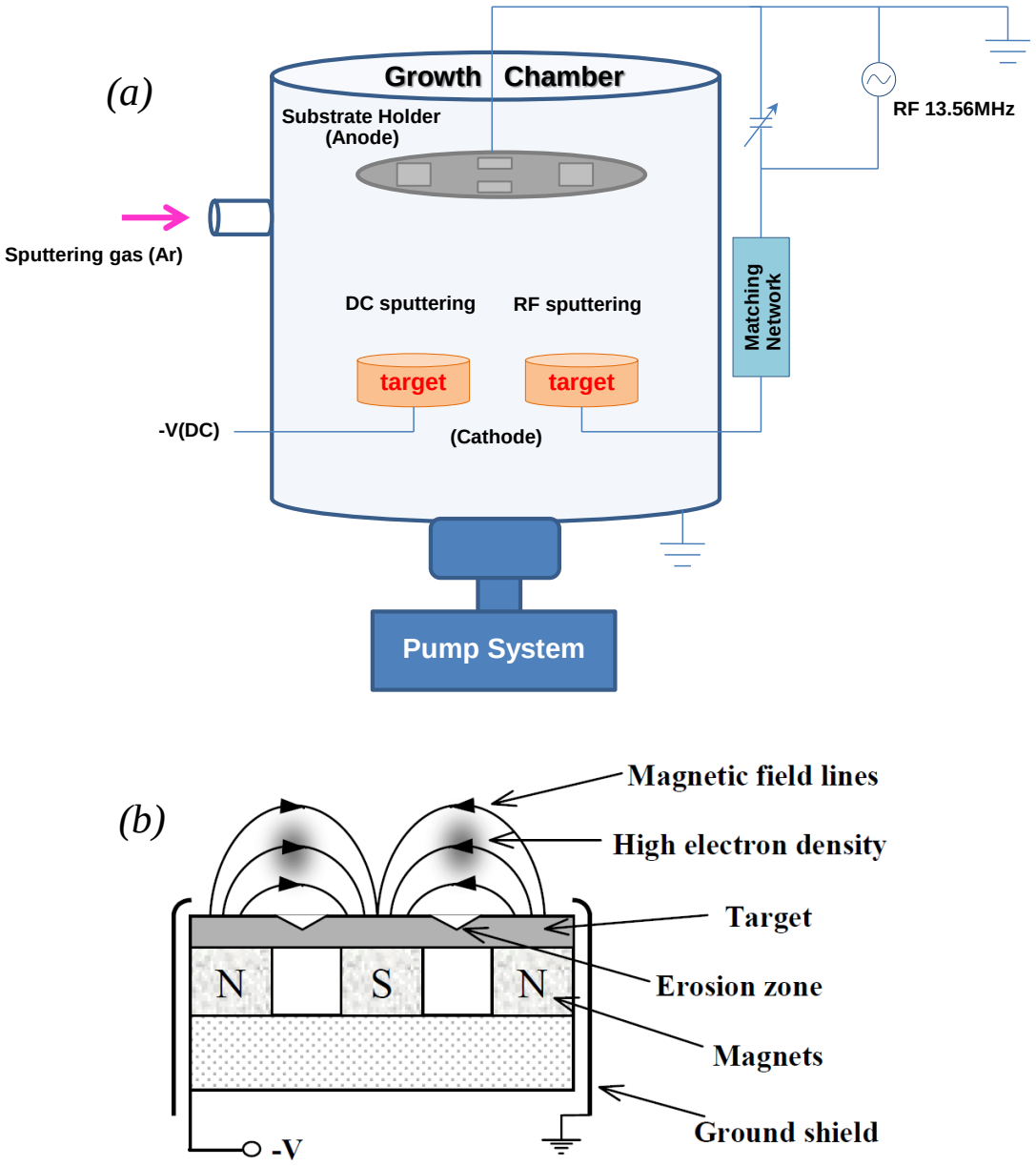


*Figure 2.9: (a) Schematics of magnetron sputtering system and (b) magnetron sputtering target*

## 2.4. Coefficient of Thermal Expansion (CTE)

The coefficient of linear thermal expansion or CTE ($\alpha$) is a physical property of material that occurs when the temperature of the body changes. Thermal expansion of material is linearly proportional to the temperature change (over some range of

temperature). This gives rise to internal stress affecting the film adhesion when the material is heated or cooled.

The coefficient of thermal expansion is defined as the fractional increase in length per unit change of temperature, which can be written as

$$\frac{\Delta l}{l_0} = \alpha \Delta T$$

$$\alpha = \frac{1}{l_0} . \frac{dl}{dT}, \qquad (2.15)$$

where $l_0$ is the original length. The unit of CTE is reciprocal temperature ($K^{-1}$).

Values of linear thermal expansion coefficient of polycrystalline metals and nonmetallic materials used as thin films or substrates are given in Table 2.2 and 2.3.

*Table 2.2: Values of thermal expansion coefficient ( $\alpha$ ) of polycrystalline metals [13].*

| Material[a] | Linear thermal expansion coefficient, $\alpha$ in units of ($10^{-6}$ °$C^{-1}$); $T$ in units of °C | Temp. range (°C) |
|---|---|---|
| W | $4.266 + 1.696\times10^{-3}(T-20) - 5.922\times10^{-7}(T-20)^2$ | 20 – 1122 |
| | $5.416 + 3.904\times10^{-4}(T-1122) + 1.327\times10^{-6}(T-1122)^2$ | 1122 – 2222 |
| | $7.451 + 3.308\times10^{-3}(T-2222) + 2.27\times10^{-7}(T-2222)^2$ | 2222 – 3327 |
| Mo | $4.697 + 1.951\times10^{-3}(T-20) + 2.821\times10^{-7}(T-20)^2$ | 20 – 1272 |
| | $7.583 + 2.658\times10^{-3}(T-1272) + 3.447\times10^{-6}(T-1272)^2$ | 1272 – 2527 |
| Al | $1.415 + 0.1615(T+268) - 2.60\times10^{-4}(T+268)^2$ | –268 – 27 |
| | $23.64 + 8.328\times10^{-3}(T-27) + 2.481\times10^{-5}(T-27)^2$ | 27 – 627 |
| Cu | $10.73 + 0.0581\ (T+173) - 1.364\times10^{-4}(T+173)^2$ | –173 – 20 |
| | $16.85 + 5.404\times10^{-3}(T-20) + 3.447\times10^{-6}(T-20)^2$ | 20 – 1027 |
| Au | $11.67 + 0.02694\ (T+173) - 6.351\times10^{-5}(T+173)^2$ | –173 – 20 |
| | $14.51 + 2.426\times10^{-3}(T-20) + 5.043\times10^{-6}(T-20)^2$ | 20 – 1027 |
| Ag | $16.47 + 7.478\times10^{-3}(T+273) + 1.885\times10^{-6}(T+273)^2$ | –73 – 927 |
| steel | $4.337 + 25.46\times10^{-3}(T+273) - 1.334\times10^{-5}(T+273)^2$ | –223 – 727 |

*Table 2.3: Values of thermal expansion coefficient ( $\alpha$ ) of nonmetallic materials [13].*

| Material[a] | Linear thermal expansion coefficient $\alpha$ in units of ($10^{-6}$ °C$^{-1}$); $T$ in units of °C | Temp. range (°C) |
|---|---|---|
| Si (100) | $3.084 + 0.00196\ T$ | 20 – 700 |
| Ge (100) | $6.05 + 0.0036\ T - 3.5\times10^{-7}T^2$ | 20 – 810 |
| GaAs (100) | $5.35 + 0.008\ T$ | 10–300 |
| C (diamond) | $0.87 + 0.00923\ T + 7\times10^{-6}T^2$ | 0 – 555 |
| polycrystalline diamond film | 2.5 | 30 – 350 |
| DLC film (diamond-like C) | 2.3 | 30 – 250 |
| TiN | $4.9 + 0.0077\ (T+273) - 2.6\times10^{-6}(T+273)^2$ | 20 – 1327 |
| polysilicon | $-0.15 - 3.1\times10^{-3}(T+273) + 4.6\times10^{-5}(T+273)^2$<br>$1.6 + 4.4\times10^{-3}(T+273) - 1.6\times10^{-6}(T+273)^2$ | –253 – 20<br>20 – 1327 |
| fused $SiO_2$ | $-1.479 + 0.0111\ (T+273) - 1.432\times10^{-5}(T+273)^2$<br>$0.3968 + 9.332\times10^{-4}(T+273) - 1.034\times10^{-6}(T+273)^2$ | –193 – 20<br>20 – 727 |
| $Ta_2O_5$ | $0.027 + 0.0094\ (T+273) - 5.4\times10^{-6}(T+273)^2$ | 25 – 937 |
| $\alpha$–SiC | $3.0 + 0.0028\ (T+273) - 4.5\times10^{-7}(T+273)^2$ | 20 – 2500 |
| $\beta$–SiC | $1.6 + 0.0042\ (T+273) - 5.9\times10^{-7}(T+273)^2$ | 20 – 900 |
| $Si_3N_4$ | $-3.4 + 0.018\ (T+273) - 1.2\times10^{-5}(T+273)^2$<br>$1.7 + 0.0024\ (T+273) - 6.3\times10^{-7}(T+273)^2$ | 20 – 227<br>227–1727 |
| $Al_2O_3$ | $-2.5 + 0.033\ (T+273) - 2.0\times10^{-5}(T+273)^2$<br>$4.5 + 0.0062\ (T+273) - 1.5\times10^{-6}(T+273)^2$ | –173 – 20<br>20–1627 |
| $ZrO_2$ | $13 - 0.018\ (T+273) + 1.2\times10^{-5}(T+273)^2$ | 20 – 1127 |
| $ThO_2$ | $5.1 + 0.0075\ (T+273) - 2.3\times10^{-6}(T+273)^2$ | –123 – 1727 |
| $Cr_2O_3$ | $10.4 - 0.0062\ (T+273) + 3.2\times10^{-6}(T+273)^2$ | 20–1127 |
| BeO | $4.4 + 0.0066\ (T+273) - 8.3\times10^{-7}(T+273)^2$ | 20–2000 |

# Chapter III

## Fabrication of CIGS thin film solar cells on glass substrates and Characterization techniques

In this chapter, I will describe the fabrication processes for standard CIGS thin film solar cells, including characterization techniques. The schematic diagram of experimental procedures is shown in Fig. 3.1.

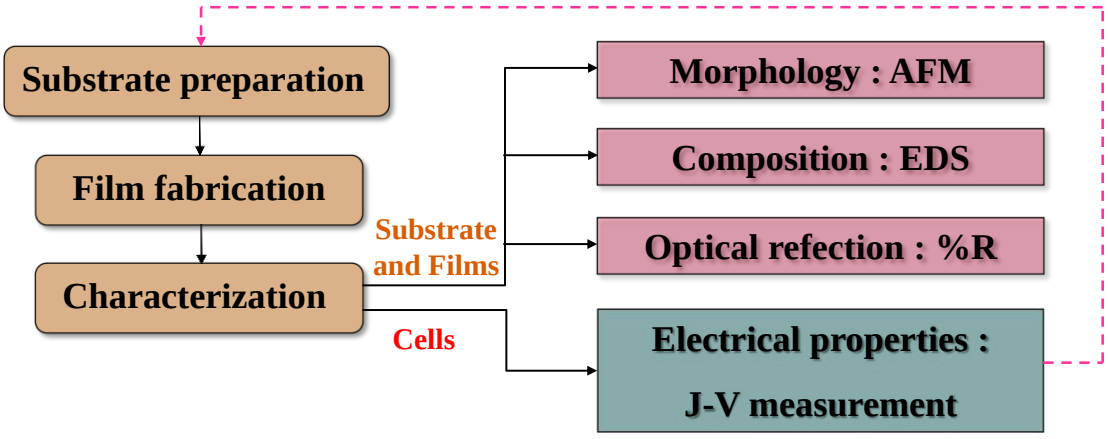


*Figure 3.1: Schematic diagrams of experimental procedures.*

## 3.1. Fabrication processes of standard CIGS thin film solar cells

The structure of standard CIGS thin film solar cells on a soda-lime glass (SLG) substrate is shown in Fig. 3.2. The Mo thin film, as a back electrode, is deposited on the SLG substrate by the DC magnetron sputtering with a thickness of 0.5 µm. The p-type CIGS thin film semiconductor is deposited by molecular beam deposition (MBD). Typically, the thickness of the CIGS films is approximately 1.5-2 µm. The n-type CdS buffer layer with a thickness of 100 nm is followed using chemical bath deposition (CBD). Then, the ZnO bilayer, as a front window, is deposited using the RF magnetron sputtering. The first layer is the thin intrinsic ZnO film with a thickness of 50 nm and the second layer is the n-type Al-doped-ZnO thin film semiconductor with a thickness of 0.5 µm. To complete the cell structure, the Al metal grid is evaporated on the topmost layer through a shadow mask with a thickness of 1.5-2 µm.

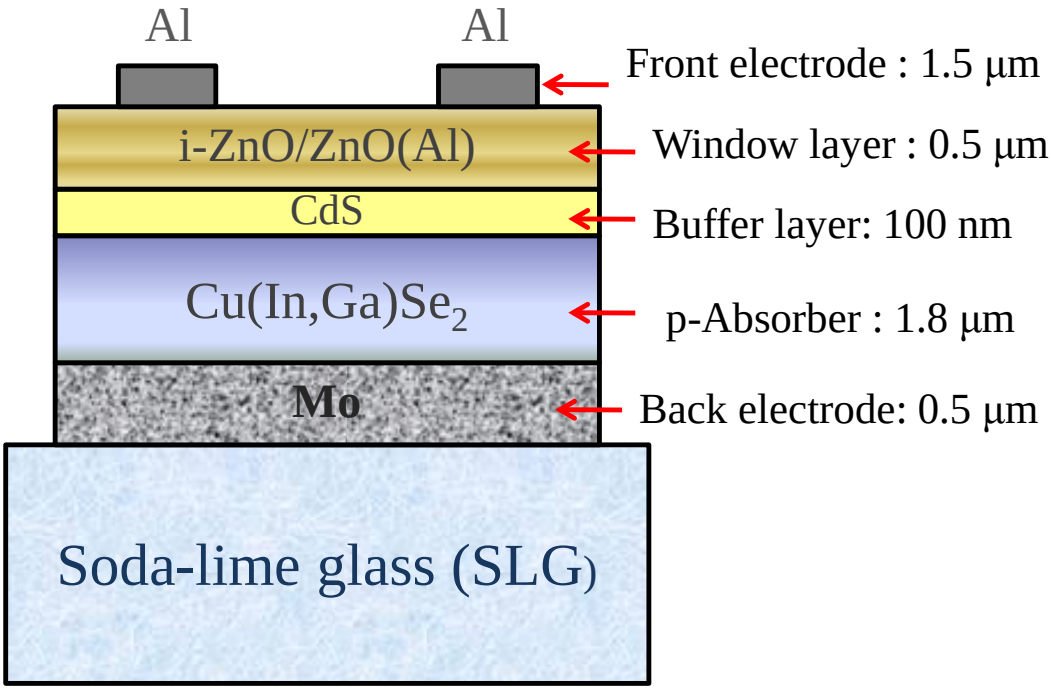


*Figure 3.2: Schematic diagram of standard CIGS thin film solar cell structure.*

The details of material physical properties and thin film preparation in each layer of CIGS solar cells on a rigid glass substrate can be described as the followings.

### 3.1.1. Mo back contact

Mo is generally used as the back contact or electrode material for CIGS thin film solar cells. The main reasons are:

- Good electrical conductivity,
- Good thermal conductivity and high melting point temperature,
- Stable under the chemical environment,

After cleaning the substrate, Mo back contact is deposited on an SLG by the DC magnetron sputtering using the 99.99% pure Mo target (4-inch in diameter) in Argon atmosphere at $6x10^{-3}$ mbar with the DC sputtering power of 550 Watt for 3 minutes using a fixed substrate holder. The distance between the substrate holder and the target is about 6 cm. The surface morphology of Mo thin film (on SLG substrate) is shown in Fig. 3.7 (a). The AFM image of Mo thin film shows the small triangle grain. And the x-ray diffraction (XRD) result shows the (110) preferred orientation of Mo thin film (in Fig. 4.10.)

### 3.1.2. CIGS absorber layer

The CIGS acts as a light absorber layer with high absorption coefficient and its direct energy band gap make it an efficient light absorber despite in the form of thin film. The CIGS absorber is deposited by a molecular beam deposition (MBD) technique. The temperature of the substrate is monitored through the pyrometer (at a wavelength of 1.55 μm) as well as the output power of the substrate temperature controller in order to achieve the end-point detection (EPD) of the process [14]. Both pyrometer and output power signals are known as the *in-situ* monitoring signals which are sensitive to the CIGS phase transformation during the growth process.

Before the growth of the film, the first step is to check the deposition rate of each source at different temperatures using quartz crystal thickness monitor (QCM). These data are used in the calculation of the source temperatures (Cu, In and Ga sources) for the CIGS growth. No rate calculation is needed for Se because it is always set at high enough flux. The calculation method is described as the followings.

### 3.1.2.1 Calculation of the CIGS deposition

The deposition rate is related to the source temperature as

$$\ln(r) = a\frac{1}{T} + b, \qquad (3.1)$$

where $r$ is the deposition rate (Å/s) of each element, i.e. Cu, In, Ga,

$T$ is the source temperature in degree Celsius ($^{o}$C),

and $a,b$ are the parameters obtained by the least-square fit method.

The examples of the plot of the deposition rate and temperature of each source are shown in Fig. 3.3

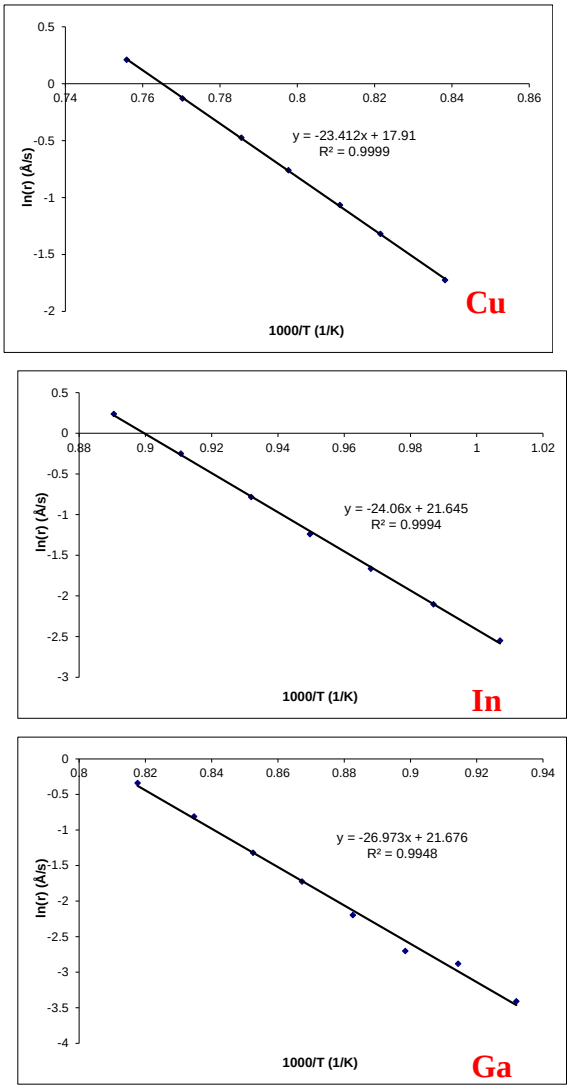


*Figure 3.3: The graphs of ln (r) vs. 1/T of Cu, In and Ga sources.*

After obtaining the fitting parameters (*a* and *b*) from Eq. (3.1), I calculate deposition rate of each element by starting to find the desired thickness of Cu ($d_{Cu}$) from Eq. (3.2)

$$\frac{d_{Cu}}{d_{CIGS}} = \frac{N_{Cu}.(M_{Cu}).[\rho_{CIS}.(1-x)+\rho_{CGS}.x]}{N_{CIGS}.[M_{Cu}+M_{In}.(1-x)+M_{Ga}.x+2.M_{Se}].(\rho_{Cu})}, \quad (3.2)$$

The deposition rates (*r*) of Cu, In and Ga can be obtained from these equations;

$$r_{Cu} = \frac{d_{Cu}}{t_{Cu}}, \quad (3.3)$$

$$r_{Ga} = \frac{x}{y}.\frac{\alpha_{Cu}}{\alpha_{Ga}}.r_{Cu}, \quad (3.4)$$

$$r_{In} = \frac{(1-x)}{y}.\frac{\alpha_{Cu}}{\alpha_{In}}.r_{Cu}, \quad (3.5)$$

where $d_{CIGS}$ is the thickness of CIGS layer (1.8 μm)

$x$ is the ratio of Ga to group three element ($\frac{[Ga]}{[Ga]+[In]}$)

$y$ is the ratio of Cu to group three element ($\frac{[Cu]}{[Ga]+[In]}$)

$t_{Cu}$ is the deposition time of Cu flux

$N_{Cu,CIGS}$ is the number of Cu atoms and CIGS molecules that is set $N_{Cu}=N_{CIGS}$

$M_i$ is the molecular mass of each element *i*

$\rho_i$ is the density of each element *i*

and $\alpha_i$ is the ratio of density to molecular mass ($\frac{\rho_i}{M_i}$)

The density and molecular mass values of the materials are given in Table 3.1

*Table 3.1: Density ($\rho$) and molecular mass (M) and $\alpha$ parameter of the CIGS materials*

| **Material** | $\rho$ **(g/cm$^3$)** | $M$**(g/mole)** | $\alpha = \rho/M$ **(mole/cm$^3$)** |
|---|---|---|---|
| Cu | 8.96 | 63.55 | 0.1410 |
| In | 7.31 | 114.82 | 0.0637 |
| Ga | 5.91 | 69.72 | 0.0848 |
| Se | 4.79 | 78.96 | 0.0607 |
| CIS | 5.89 | 336.29 | - |
| CGS | 5.27 | 291.19 | - |

One needs to substitute the deposition rate value and the fitting parameters of each element into Eq. (3.1) again in order to find the working temperatures of the sources during the deposition process. The details for the deposition of the CIGS layer in the two-stage and three-stage processes are described as followed.

#### 3.1.2.2 Two-stage process

In the first stage, the precursor layer is deposited with Cu-rich composition ($y$>1) and then followed by the deposition of layer with only In, Ga and Se in the second stage until the chalcopyrite phase or α-CIGS phase (y≤1) is obtained. The substrate temperature is set at 540$^o$C. The surface morphology of CIGS films from the two stage process typically shows larger grain size and rougher surface compared with other processes due to the influence of $Cu_{2-x}Se$ liquid phase in the first stage. $Cu_{2-x}Se$ covers the CIGS surface and diffuses into the CIGS grain boundary leading to the formation of large CIGS grain [15]. Figure 3.4 shows the growth profile and the film composition of CIGS in the two-stage process. The relationship between the evolution of the film composition and the deposition time can be written as

$$y(t_1).t_1 = y(t_2).t_2, \qquad (3.6)$$

where $y(t_1)$ and $y(t_2)$ are the values of y ratio at the desired deposition time in the first stage ($t_1$) and the second stage ($t_2$), respectively.

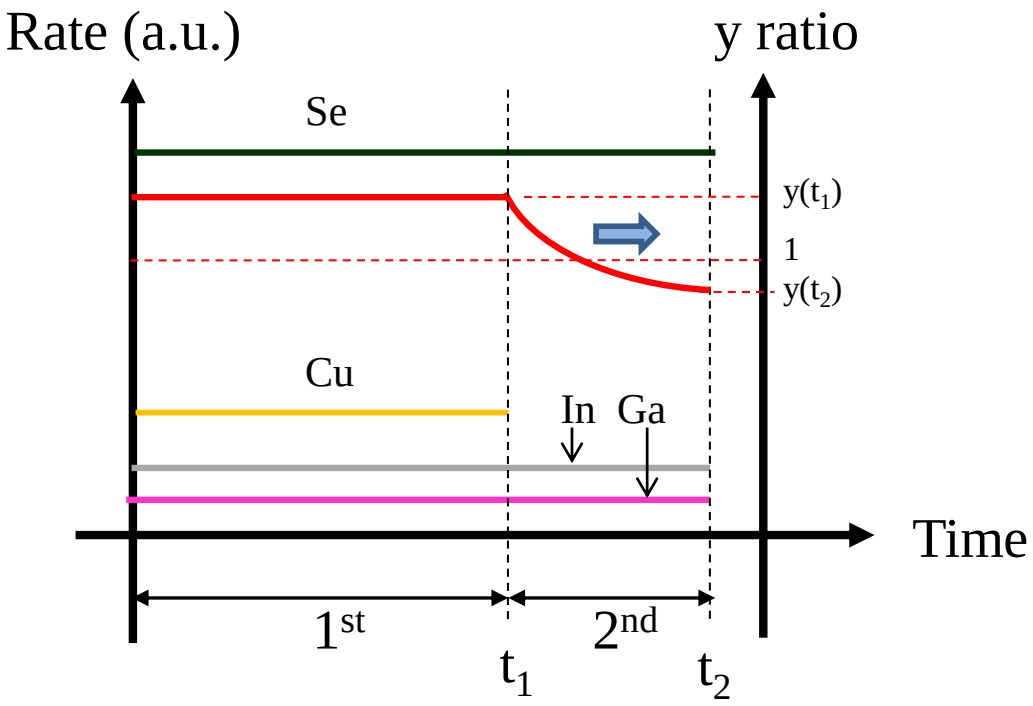


*Figure 3.4: Schematic of the growth profile and the film composition of the two-stage process.*

*Table 3.2: Required data for the 2-stage process (by using the fitting parameter in Fig. 3.3)*

| Required Data | |
|---|---|
| $d_{CIGS}$ | 1.8 µm |
| $t_{Cu,1}$ | 2700 sec |
| $x$ | 0.3 |
| $y(t_1)$ | 1.2 |

Example of temperature setting for the sources in the 2-stage process is given in Table 3.3:

*Table 3.3: Calculated data from Table 3.2*

| Calculated data | |
|---|---|
| $d_{cu}$ | 0.225 μm |
| $r_{cu}$ | 0.84 Å/s |
| $r_{In}$ | 1.08 Å/s |
| $r_{Ga}$ | 0.35 Å/s |
| $T_{cu}$ | 1021$^{o}$C |
| $T_{In}$ | 842$^{o}$C |
| $T_{Ga}$ | 913$^{o}$C |

#### 3.1.2.3 Three-stage process

The three-stage process is a method for CIGS thin film deposition that generally yields the highest cell efficiency when compared with the two-stage process and other methods. In the first stage, the precursor layer is deposited with high rate of In and Ga without Cu flux or $y$=0. The second stage, only the Cu flux is allowed on the precursor layer in order to obtain the Cu-rich composition. Finally, the composition is converted into the Cu-poor (with low rate of In and Ga) in the third stage by terminating the Cu flux and the growth profile is the same as in the first stage. The substrate temperature is set at 400$^{o}$C in the first stage and 540$^{o}$C in the second and the third stages. The surface morphology of the CIGS films from the three-stage process shows the smoother surface [15] than those films grown by the two-stage process. The surface morphology affects the junction formation with the CdS buffer layer. The growth profile and the evolution of film composition in the three-stage process are shown in Fig. 3.5. The calculation of the composition and deposition time during the 1$^{st}$ and the 2$^{nd}$ stage of the three-stage process can be written as

$$\frac{y(t_1)}{t_1} = \frac{y(t_2)}{t_2}, \qquad (3.7)$$

Eq. (3.7) can be used to evaluate the film composition in the second stage due to the $y$ ratio increases with the deposition time whereas the composition in the third stage decreases with the deposition time which is the same as the two-stage process in

Eq. (3.6). The surface morphology of the 3-stage-CIGS film (on Mo/SLG substrate) is shown in Fig. 3.7 (c).

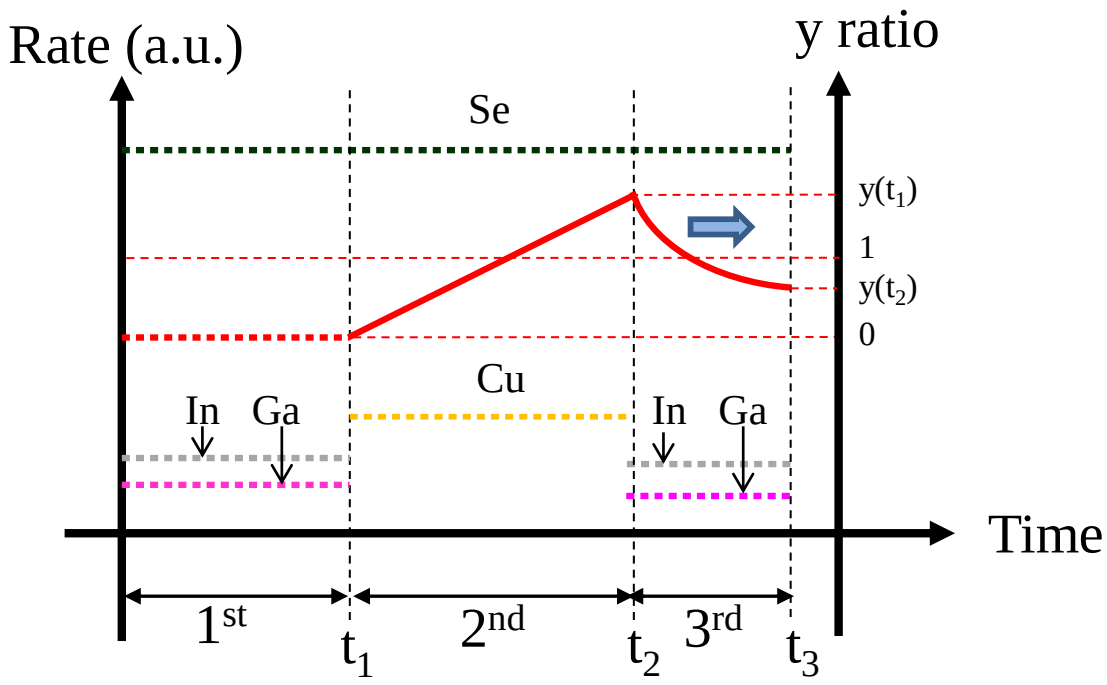


*Figure 3.5: Schematic representations of the growth profile and the film composition for the three stage process.*

*Table 3.4: Required data for the 3-stage process*

| Required Data | |
|---|---|
| $d_{CIGS}$ | 1.8 µm |
| $t_{Cu}$ | 1800 sec |
| $t_{1,3}$ | 1800, 2700 sec |
| $x$ | 0.37 |
| $y(t_2)$ | 1.3 |

Example of temperature setting for the sources in the 3-stage process is given in Tables 3.4 and 3.5, where $t_{1,3}$ is the deposition time of group III (In and Ga) for high rate in the first stage and low rate in the third stage, respectively. The calculation of the temperature of In and Ga sources in the three-stage process is a different from the two-stage process that is set $t_{Cu}=t_{1,3}$ in Eq. (3.3).

*Table 3.5: Calculated data from Table 3.4*

| Calculated data | |
|---|---|
| $d_{cu}$ | 0.23 µm |
| $r_{Cu}$ | 1.26 Å/s |
| $r_{In}$ | 1.35,0.9 Å/s |
| $r_{Ga}$ | 0.59, 0.4 Å/s |
| $T_{cu}$ | 1051$^{o}$C |
| $T_{In}$ | 854, 833$^{o}$C |
| $T_{Ga}$ | 942, 920$^{o}$C |

### 3.1.3. CdS buffer layer

The p-n heterojunction of the CIGS thin film solar cell is established by the formation of the p-type CIGS absorber layer and the n-type ZnO(Al) window/CdS buffer layers. CdS has a direct band gap of 2.4 eV. Thus, the photon energy more than 2.4 eV or the blue region of the visible spectrum is partially absorbed in this layer, but it cannot generate the photocurrent due to the short diffusion length of minority carrier or holes in the n-type CdS layer leading to the recombination or the loss of current. CdS buffer layer is deposited by using chemical bath deposition (CBD). This deposition can completely cover on the rough CIGS surface in order to prevent the damage of the CIGS surface and create the shunting between the ZnO and the CIGS layers. The CdS solution can also remove oxide layers on the CIGS surface for the good junction formation.

Table 3.6 shows the parameters of the CdS solution used in this work. The CdS solution is a mixture of DI water, $CdSO_4$ solution, ammonia solution (complex agent) and $SC(NH_2)_2$ solution in the beaker (600 ml), respectively. The beaker is placed in a water bath at the temperature of 65$^{o}$C. During the deposition, the solution is stirred (150 rpm) in order to obtain the homogeneous of temperature and concentration of CdS solution. After the deposition, the sample is rinsed in DI water and blown dry with nitrogen gas.

*Table 3.6: Parameters of the CdS condition*

| Cd source $CdSO_4$ | S source $SC(NH_2)_2$ | Complex $NH_4OH$ | DI water | Temp ($^oC$) | Time (min) |
|---|---|---|---|---|---|
| 27 mM (0.3456 g) in 50 ml DI water | 37.5 mM (2.85 g) in 100 ml DI water | 80 ml | 270 ml | 65 | 14 |

The deposition of CdS thin film can be described by these reactions:

i) Release of $Cd^{2+}$ from the ammonia solution;

$$Cd(NH_3)_4^{2+} \longrightarrow Cd^{2+} + 4NH_3, \quad (3.8)$$

ii) Release of $S^{2-}$ from thiourea;

$$SC(NH_2)_2 + 2OH^- \longrightarrow S^{2-} + CH_2N_2 + 2H_2O, \quad (3.9)$$

iii) Precipitation of CdS;

$$Cd^{2+} + S^{2-} \longrightarrow CdS(s), \quad (3.10)$$

The CdS thin film can be formed with three different mechanisms [16]. In the first stage, the film is formed with low rate or nucleation growth. Second, the reaction of $Cd^{2+}$ and $S^{2-}$ ions will occur at the CIGS surface with higher rate or ion by ion growth. Third, the precipitation of collides in the CdS solution or heterogeneous growth.

### 3.1.4. ZnO window layers

The bilayer ZnO window are the transparent conducting oxide (TCO) materials with high transparency (or low absorption) which allow the incident light to pass through and provide good electrical conductivity for the photocurrent into the metal grid and external circuit. The ZnO bilayer consist of the undoped intrinsic ZnO (i-ZnO) and Al-doped ZnO (ZnO(Al)). They are the direct band gap semiconductors. The energy band gaps of i-ZnO and ZnO(Al ) are about 3.3 and 3.6-3.8 eV, respectively.

After the buffer layer deposition, the i-ZnO thin film is deposited by the RF magnetron sputtering using the ZnO ceramic target (2-inch in diameter) in Argon atmosphere at $6x10^{-3}$ mbar with the sputtering power of 80 Watt for 11 minutes. The distance between a substrate holder and a target is about 6 cm and the substrate holder is rotated at 10 rpm in order to allow the relaxation of the film. The functions of the first i-ZnO layer are to prevent the shunting due to its high resistivity from the CdS layer and adjust the band alignment for the suitable formation of the p-n junction.

The deposition of ZnO(Al) is then followed as the second layer by the RF magnetron sputtering using the ZnO target with 2wt% $Al_2O_3$ (4-inch in diameter) in Argon atmosphere at $3x10^{-3}$ mbar with the sputtering power of 220 Watt for 80 minutes. The distance between a substrate holder and a target is about 6 cm and the substrate holder is rotated at 3 rpm. This layer provides good conductivity and high carrier concentration. The surface morphology of ZnO(Al) film on SLG substrate is shown in Fig. 3.7 (b).

### 3.1.5. Al metal grid

Al grid serves as the front contact/electrode in order to facilitate current collection due to it has a good electrical conductivity. Metal grid is deposited by using the thermal evaporation through a shadow mask at the base pressure of $6x10^{-6}$ mbar. The film thickness and deposition rate are controlled by the oscillating quartz crystal monitor (QCM). The thickness of Al layer is approximately 1.5-2 μm.

## 3.2. Thin film characterization techniques

In this section, I will describe about characterization techniques for thin films and device performance; atomic force microscopy (AFM), X-ray diffraction (XRD), optical refraction spectroscopy, and current-voltage (J-V) measurement.

### 3.2.1. Atomic Force Microscopy (AFM)

The atomic force microscope or scanning force microscope is an instrument that is used to analyze and characterize surface morphology of both conducting and non-conducting materials in micro down to nano scales. The AFM consists of the

piezoelectric scanner, a laser source, the photodiode detector and a sharp tip that is attached to the end of the cantilever.

The AFM operates by scanning a sharp tip on the sample surface and generating the deviation of the cantilever from the interaction force between the tip and the sample surface. The deviation of the cantilever is measured by using the refection of a laser beam which is transferred to photodiode detector in order to access the data processing and generate a map of surface topography. The schematic representation of the operation principles is shown in Fig. 3.6. The surface morphologies of the films fabricated in this work; Mo, CIGS, ZnO, are given as examples in Fig. 3.7.

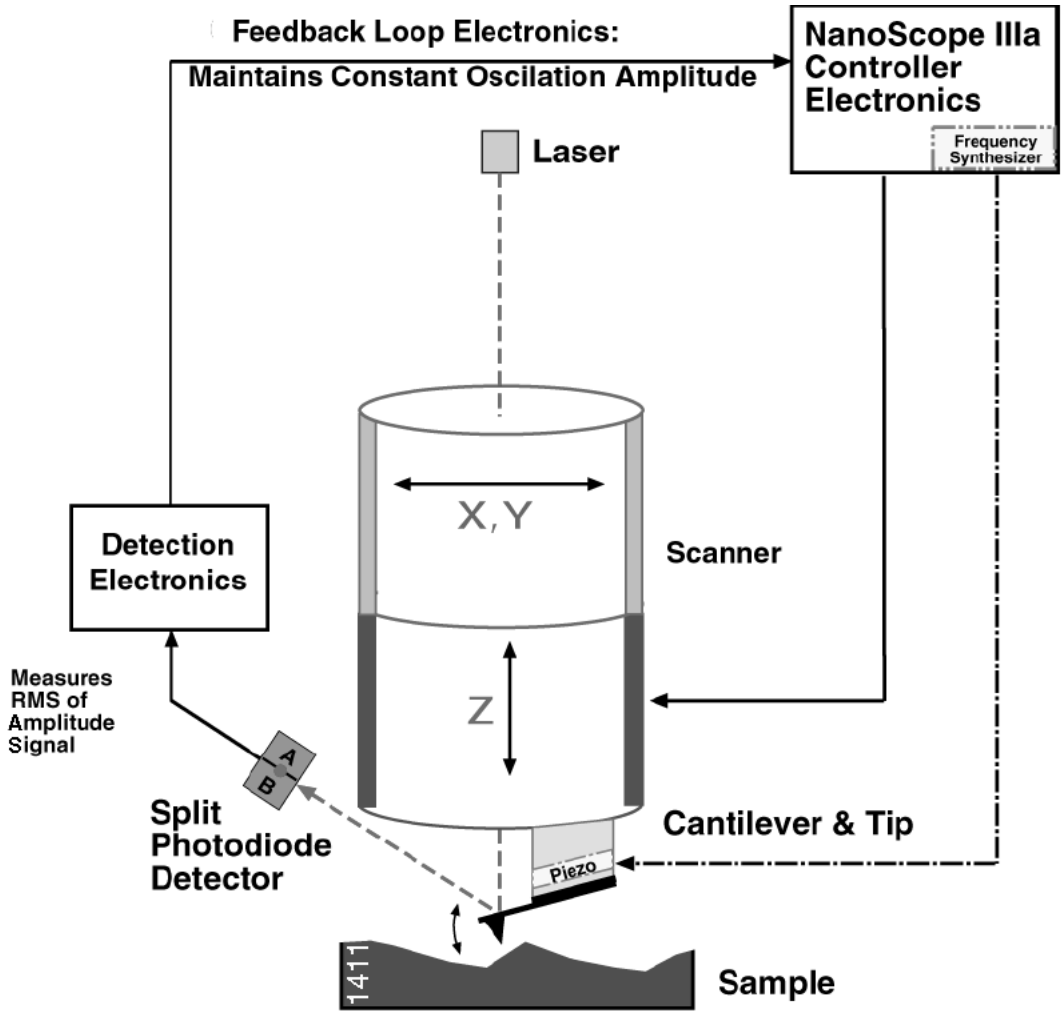


*Figure 3.6: Operation loop of the tapping mode AFM system [17].*

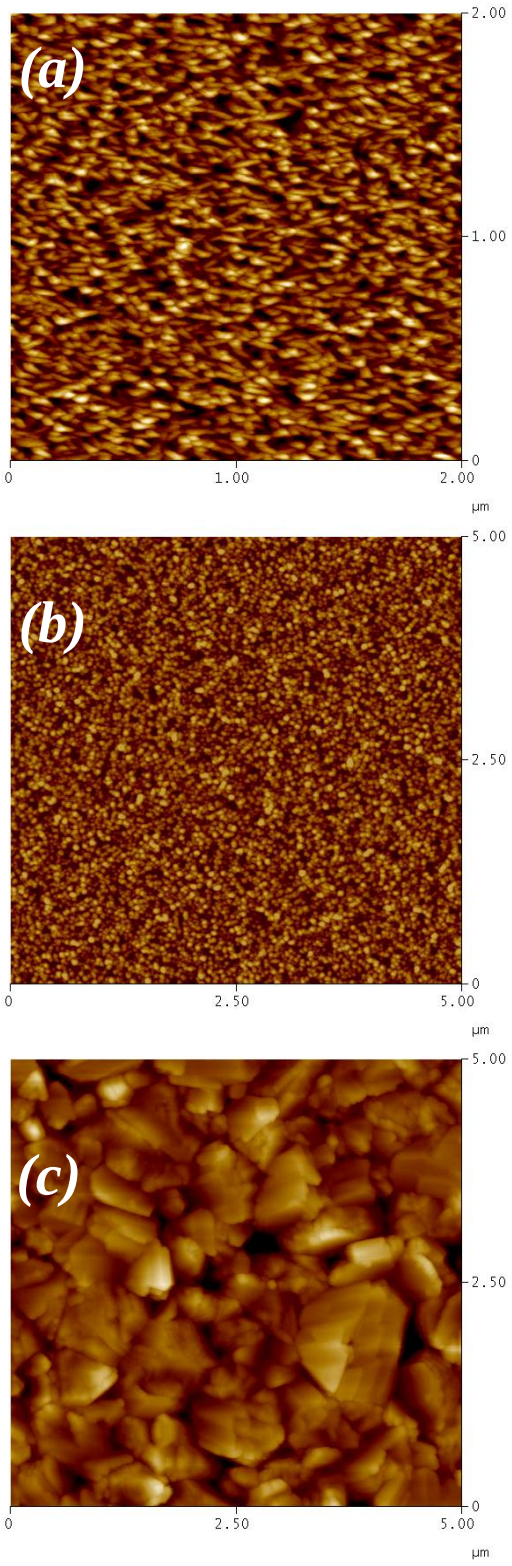


*Figure 3.7: Examples of AFM images showing surface of a) Mo film b) ZnO(Al) film and c) CIGS film in 3-stage process.*

### 3.2.2. X-ray diffraction (XRD)

The X-ray diffraction technique is used to characterize the crystal structure or phase of the CIGS films. X-ray incidents on the sample and is scattered from crystal lattice of sample obeying Bragg condition. The X-ray peak from the scattering is fitted by using Gaussian equation and one can find the relationship between the full width at half maximum (FWHM) and the standard deviation (σ) of X-ray peak from equation

$$FWHM = 2\sqrt{2\ln 2}\sigma. \tag{3.11}$$

The grain size (G) of the film can be calculated by using the Scherrer equation:

$$G = \frac{0.9\lambda}{FWHM\cos\theta}, \tag{3.12}$$

where λ is the X-ray wavelength (1.5406 Å for $Cu_{K\alpha 1}$ radiation) and θ is the Bragg angle in degree.

### 3.2.3. Optical reflection spectroscopy

The optical property of thin film is characterized by Perkin-Elmer Lambda 900 UV-VIS-NIR spectrophotometer in the wavelength from 200 nm to 2000 nm. The optical reflectance (*R*) can be explained by the ratio between the intensity of the reflected light ($I_R$) that depends on the film roughness and the incident light ($I_o$) from the light source by

$$R = \frac{I_R}{I_o}. \tag{3.13}$$

The thickness of the film (*d*) on the substrate can be determined from the interference fringes of reflection spectra:

$$d = \frac{M\lambda_1\lambda_2}{2n\left|(\lambda_1 - \lambda_2)\right|}, \tag{3.14}$$

where *M* is the number of cycles observed from wavelength $\lambda_1$ to $\lambda_2$ and *n* is the index of refraction of the film. The number of interference fringes increase with the film thickness. The interference fringes disappear when the wavelength of incident light is in the region near the energy band edge ($E_g$) of the film.

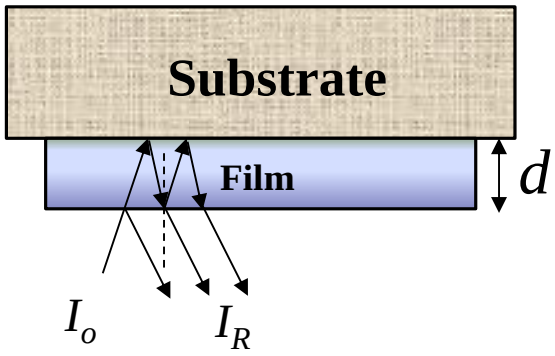


*Figure 3.8: Schematic of multiple reflections measurement of thin film.*

### 3.2.4. J-V measurement

The solar cell performance is measured by using current–voltage (J-V) measurement system under AM 1.5 and 0.1 Watt/cm$^2$ irradiance at 25°C that consists of the tungsten-halogen light source (300W-ELH lamp), the DC power supply and a voltage source/current measurement unit (Keithley model 237). The solar cell is contacted with two-point probe configuration. Data signals are transferred to a PC via IEEE-488 card in order to evaluate solar cell parameters, e.g. open-circuit voltage ($V_{oc}$), short-circuit current density ($J_{sc}$), fill factor ($FF$), series resistance ($R_s$), shunt resistance ($R_{sh}$) and solar cell efficiency ($\eta$). The schematic diagram of the J-V measurement is shown in Fig. 3.9.

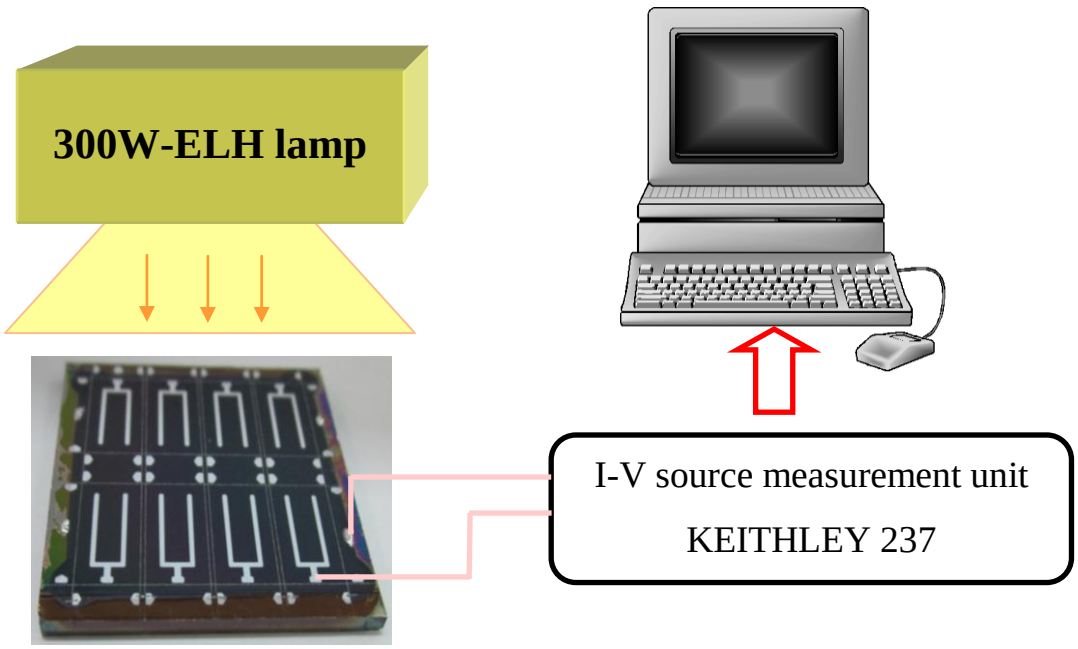


*Figure 3.9: Schematic diagram of the J-V measurement system.*

# Chapter IV

# Flexible CIGS thin film solar cells

In this chapter, the details of the fabrication processes and discussion of the results of solar cell devices on the stainless steel (SS) foil including the influences of substrate temperature during the CIGS growth, thickness of $Al_2O_3$ films and Na incorporation are given, respectively.

## 4.1. Substrate Preparation

In this of work, a 0.1 mm thick stainless steel (SS) with the area of 3x3 $cm^2$ is used as a substrate for flexible CIGS thin film solar cells. Processes for cleaning metallic substrate can be described as the followings:

1. The stainless steel substrates are scrubbed with cellulose sponge in the mixture of dishwashing liquid and de-ionized (DI) water and then blown dry with nitrogen gas in order to remove grease and dust particles on the SS surface from the manufacturing process.

2. They are thoroughly cleaned in an ultrasonic bath with Trichloroethylene (TCE) for 30 minutes in order to remove grease or any other organic substances.

3. They are then followed by the cleaning in an ultrasonic bath with acetone for 30 minutes to remove residual TCE and any organic substances.

4. Next, they are cleaned in an ultrasonic bath again with methanol for 30 minutes to remove residual acetone and any organic substances.

5. For the last wet cleaning process, they are cleaned in an ultrasonic bath with de-ionized (DI) water for 30 minutes to remove residual methanol. After that, the substrates are blown dry with nitrogen gas

6. Finally, they are heated at 200$^{o}$C for 1 hour in the furnace in order to remove humidity on the substrate surface. The clean substrates are kept in a dry cabinet before the deposition in vacuum chamber.

## 4.2. Fabrication process of flexible CIGS thin film solar cells

Figure 4.1 shows the structure of flexible CIGS solar cell on SS foil substrate that is similar to that on the SLG substrate described in chapter III. The fabrication of flexible CIGS thin film solar cells on the metallic substrate especially SS or alloy steel requires the additional of an insulating or a diffusion barrier layer before the CIGS deposition in order to prevent the diffusion of undesired elements from the substrate into the CIGS absorber layer. The $Al_2O_3$ thin film is chosen as a diffusion barrier layer in this work.

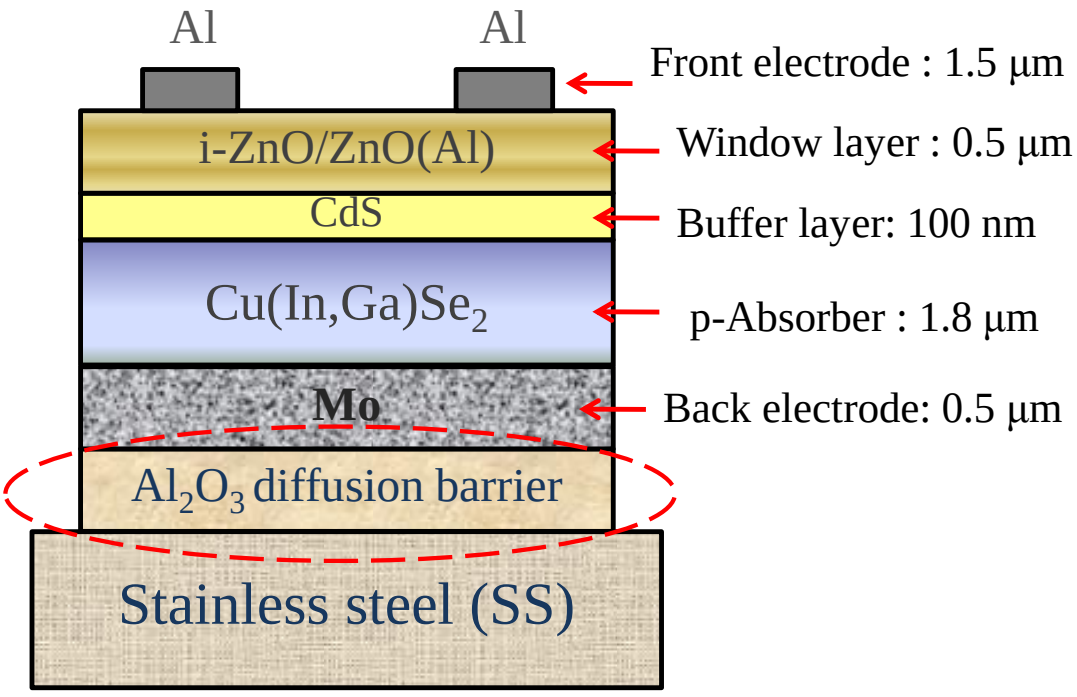


*Figure 4.1: Schematic diagram of the structure of flexible CIGS thin film solar cell on SS substrate.*

Figure 4.2 shows the fabrication process for the flexible CIGS thin film solar cells. The sample consists of 8 cells on a 3x3 $cm^2$ substrate. The total area of each cell is about 0.515 $cm^2$.

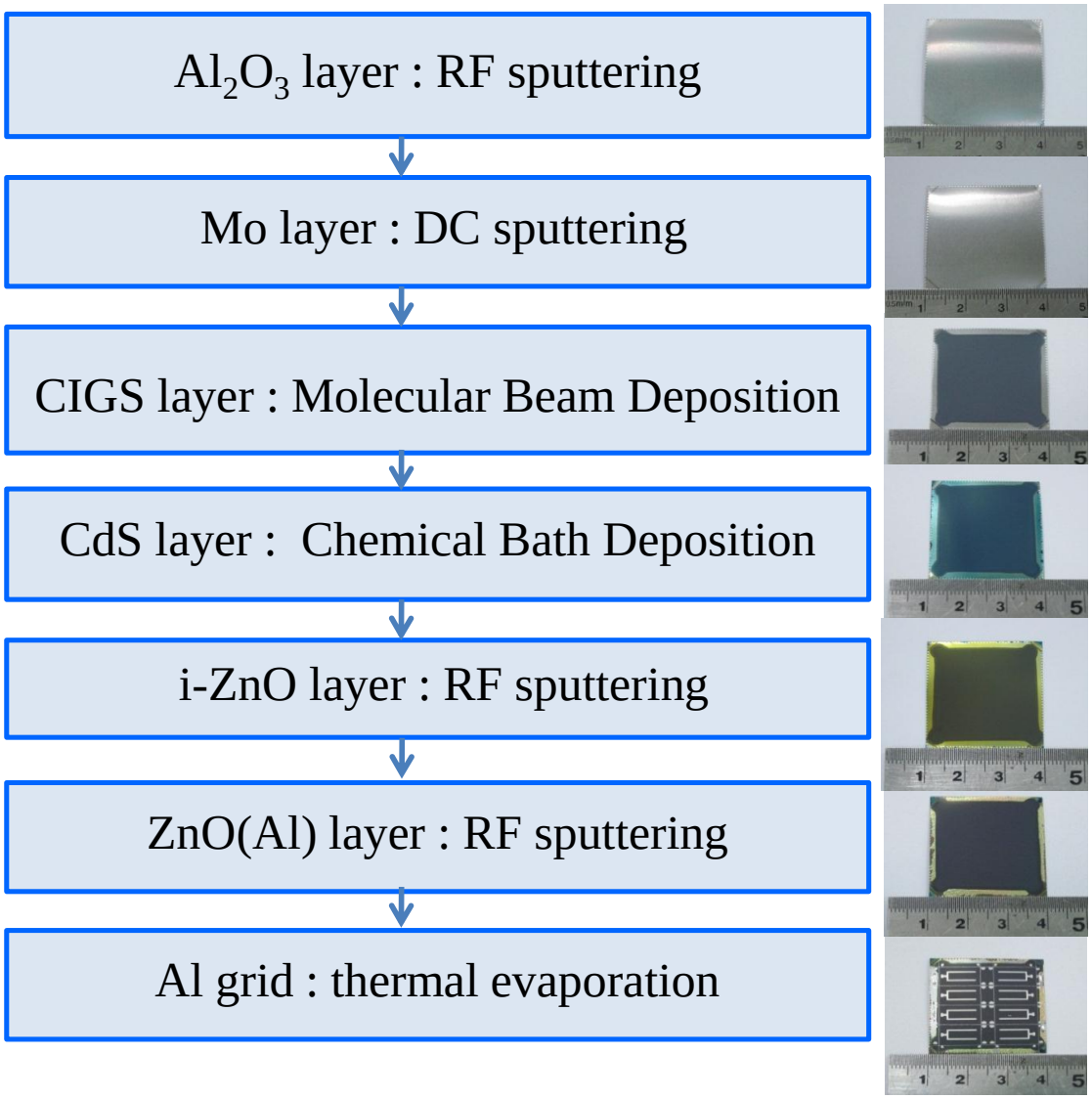


*Figure 4.2: Schematic diagram of the solar cell fabrication process on flexible substrate*

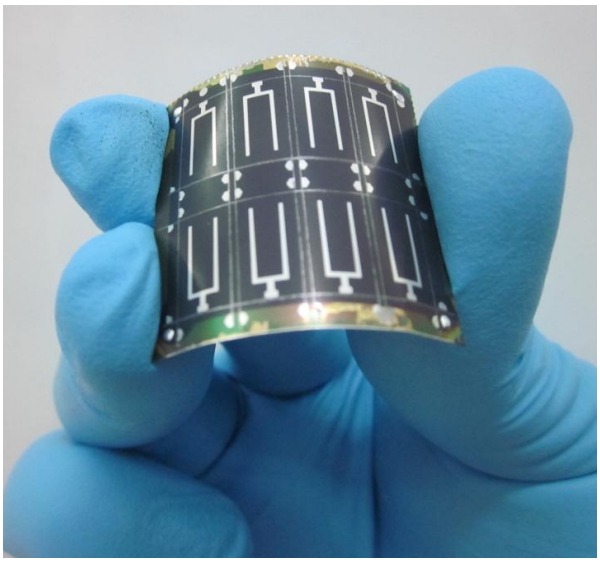

*Figure 4.3: Picture of the flexible CIGS thin film solar cells on a SS foil fabricated at Semiconductor Physics Research Laboratory (SPRL)*

## 4.3. Substrate type

SS foils; type 301, 316L and 430 are chosen as trial flexible substrates. The details of physical properties of each type of SS substrates are given in Table 4.1. The austenitic steels or SS series 300 fail during the CIGS co-evaporation process due to their too high CTE leading to CIGS adhesion problems. In addition, the $Al_2O_3$ layer can lose the ability to block impurity diffusion that is caused by cracking and delamination of films at high temperature. Figure 4.4 shows the delamination of thin films due to an unequal elongation in each side from manufacturing process.

*Table 4.1: Physical properties of the stainless steel [18]*

| **Type** | **Density ($g/cm^2$)** | **Thermal Conductivity (W/m.K) at 500$^oC$** | **Coefficient of Thermal Expansion (µm/m.K) at 500$^oC$** |
|---|---|---|---|
| 301 | 7.88 | 21.4 | 18 |
| 316L | 7.99 | 21.4 | 17 |
| 430 | 7.74 | 26.3 | 11 |

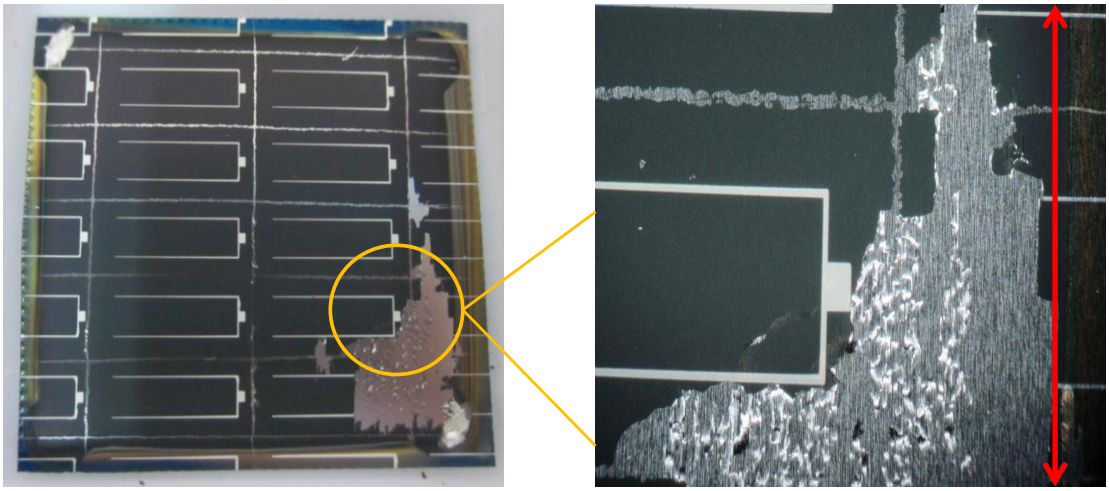

*Figure 4.4: Photograph of adhesion problem between films and SS substrate type 301.*

Therefore, SS foil type 430 is chosen as the flexible substrate in this work. Figures 4.5 and 4.6 show the SEM image and EDS spectra of the SS substrate type 430. It can be seen that the SS has rough surface and the main composition of SS substrate used in this work consists of Fe (81 At%) and Cr (19 At%). Fe and Cr also have high diffusion rate at high temperature. Thus, they could cause the degradation of the CIGS quality in the deposition process and lead to the reduction of solar cell efficiency.

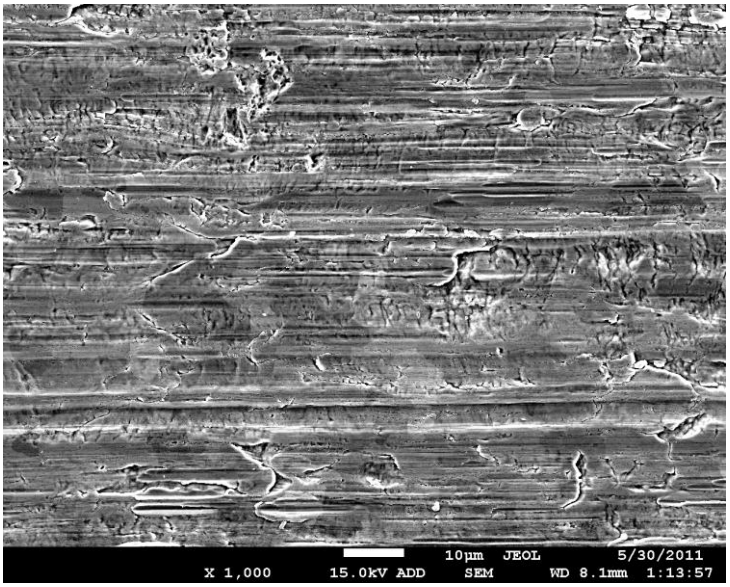


*Figure 4.5: SEM micrograph of surface of SS (type 430).*

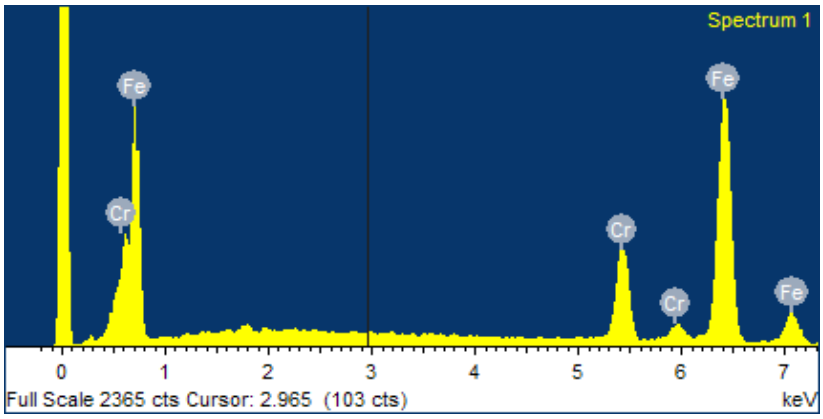


*Figure 4.6: EDS spectrum of stainless steel (type 430).*

## 4.4. Two-stage deposition process for CIGS on flexible SS

### 4.4.1. Two-stage process or bilayer process

The two-stage process is started with the Cu-rich composition, i.e. $\frac{[Cu]}{[Ga]+[In]}$ ratio or y ~ 1.2 in the first stage, and then followed by the deposition of only In, Ga and Se in the second stage until the overall composition is slightly Cu-deficient (y ~ 0.9) at the end point, i.e. the film becomes Cu-poor. The substrate temperatures are varied at about 470°C (low temperature) and 530°C (high temperature) without Na enhancement in order to study the effect of substrate temperature to the CIGS growth. The $\frac{[Ga]}{[Ga]+[In]}$ ratio (x) is set at 0.3 in order to have $E_g$ ~ 1.24 eV for the CIGS. The growth process time is about 60 minutes for the Mo/SS and Mo/400-nm-thick $Al_2O_3$/SS substrates. Figure 4.7 shows the growth profile and the film composition of CIGS in this condition for the two-stage process.

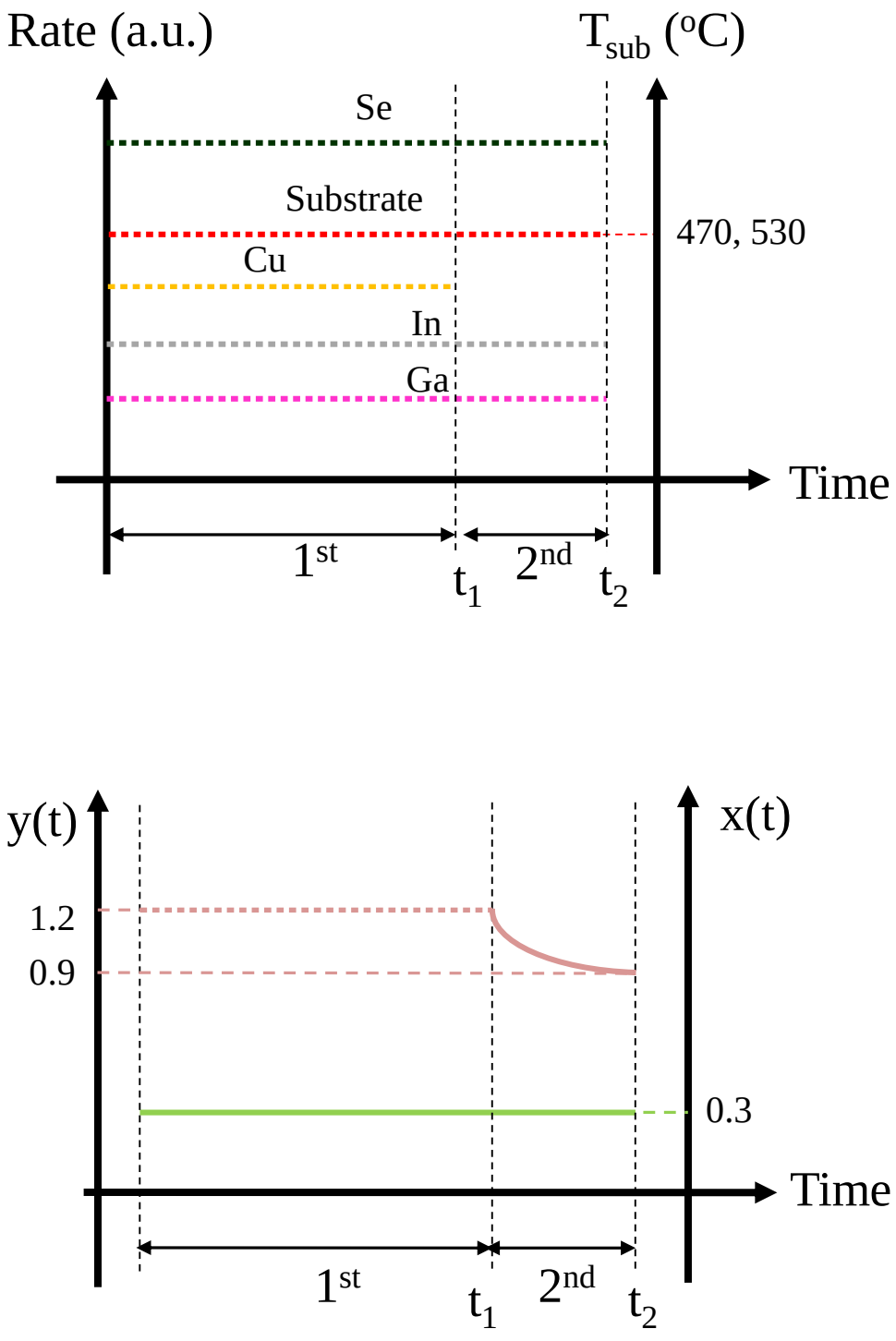


*Figure 4.7: Schematic representations of the growth profile and the film composition for the two-stage process.*

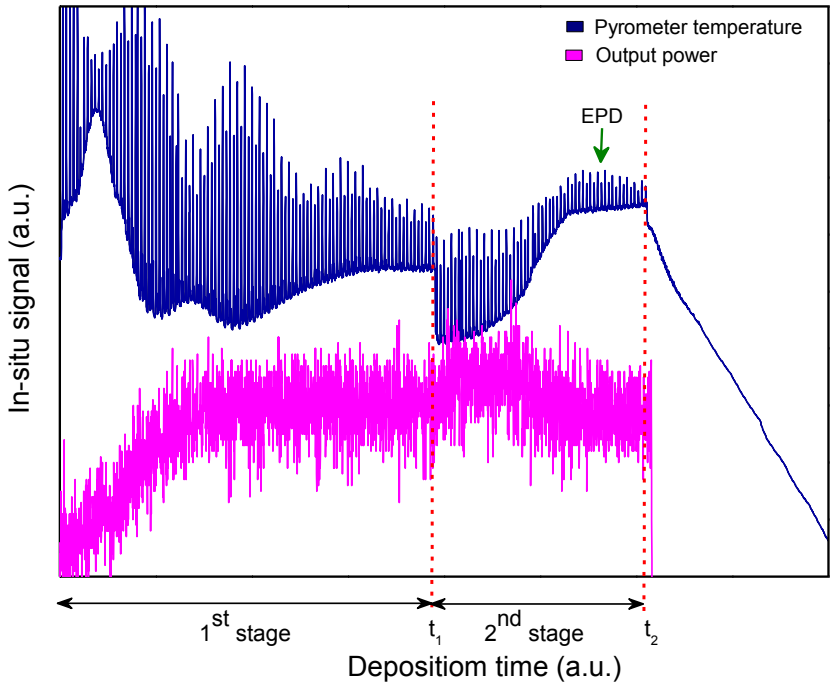


*Figure 4.8: The in-situ monitoring signals for the two-stage process.*

Figure 4.8 shows the pyrometer signal from CIGS surface temperature and output power signal of the substrate heater for the two-stage process. The low frequency oscillations of the pyrometer signal are the interference of the signals from the top and the bottom surfaces due to the increasing thickness of the film, while the high frequency oscillations correspond to the substrate rotation. The interference fringes are only observed in the Cu-rich phase and the amplitude damping during the first stage is, by nature, due to the increasing in the surface roughness of the growing film. The pyrometer signal shows a sharp drop when the Cu flux is terminated indicating the end of the first stage is caused by the change of irradiation from the surface of the CIGS film. Then the temperature starts to rise from the change in the emissivity of the film due to the evolution of the composition of the CIGS changing from Cu-rich phase to stoichiometric and eventually level off toward the Cu-poor phase at $y \sim 0.9$ or end-point-detection (EPD) that can be observed from sharp knee of pyrometer and output power signals.

### 4.4.2. Effect of substrate temperature

The experiment is also carried to observe the effect of the substrate temperature on the followings;

***Surface Morphology and Crystal Structure***

It has been noticed that the substrate temperature is one of main factors affecting CIGS growth as shown by the AFM images in Fig. 4.9. The AFM images suggest that the substrate temperature has a direct effect on the grain size and the quality of the CIGS films. The smaller grain size typically results in the decrease of diffusion length of the photo-generated charge carriers and the increase of the carrier recombination rate at the grain boundaries. The CIGS film on the Mo/SS substrate shows the largest grain as shown in Fig. 4.9 (a) for high temperature growth when compared to the film on the substrate with $Al_2O_3$ blocking layer at same substrate temperature (530$^o$C) in Fig. 4.9 (b).

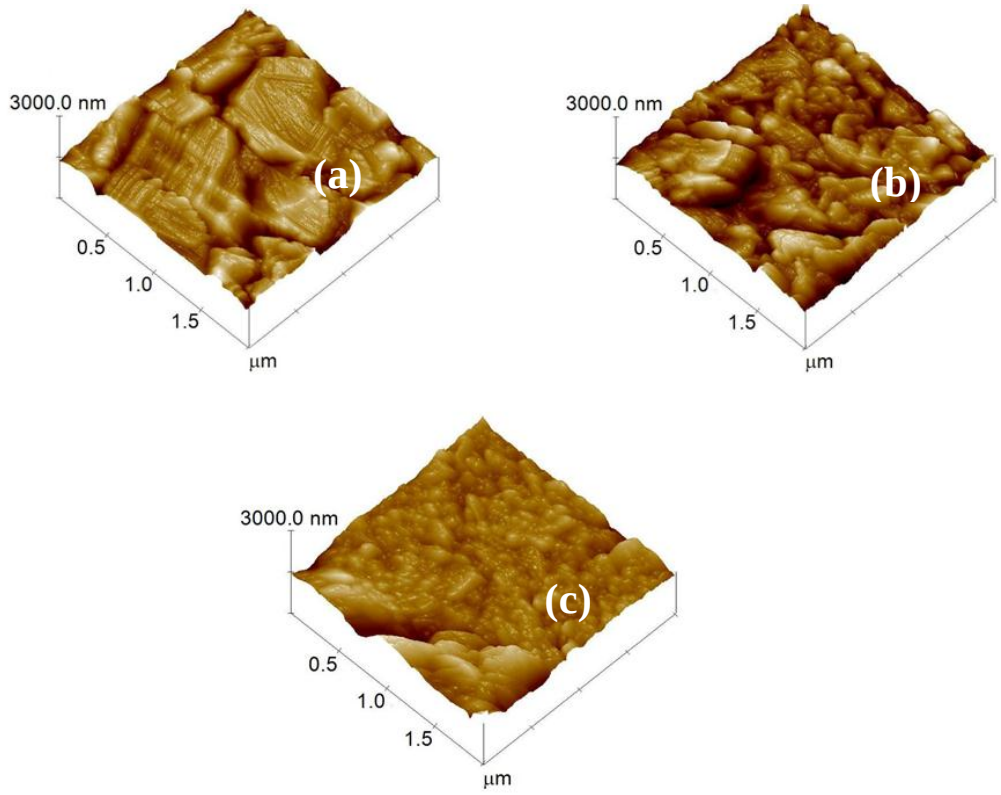


*Figure 4.9: AFM images (over 2 µm x 2 µm) of CIGS films on (a) Mo/SS substrate at 530°C, (b) Mo/400-nm-$Al_2O_3$/SS substrate at 530°C and (c) Mo/400-nm-$Al_2O_3$/SS substrate at 470°C by two-stage process*

The XRD patterns for the films with and without $Al_2O_3$ barrier at the substrate temperatures of 470°C and 530°C are compared and shown in Fig. 4.10. The intensity of (112) preferred-orientations of the CIGS films decrease when the $Al_2O_3$ film is used as a barrier layer. The important parameters extracted from the XRD are summarized in Table 4.2. The FWHM of the (112) peak is smallest for the film on the Mo/SS substrate indicating the largest grain consistent with the AFM image in Fig. 4 (a), while the FWHM of the (112) peak of the films on Mo/$Al_2O_3$/SS substrates increases with the decreasing substrate temperature resulting in the smaller grains as shown in Fig. 4.10 (b) and (c). It is worth to note here that the slight shift of XRD spectra toward the higher 2θ is observed when compared to the bulk CIGS which is due to the tensile strain caused by the anisotropic property of the SS.

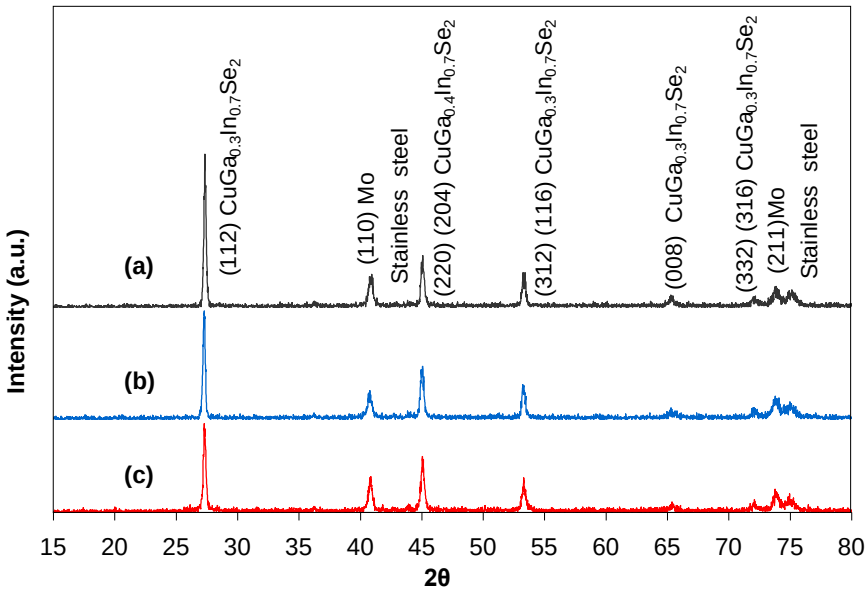


*Figure 4.10: XRD patterns of (a) CIGS 530°C/Mo/SS, (b) CIGS 530°C/Mo/400-nm-$Al_2O_3$/SS and (c) CIGS 470°C /Mo/400-nm- $Al_2O_3$/SS.*

*Table 4.2: XRD results of CIGS films on different substrates and temperatures*

| Substrate | $T_{sub}$ (°C) | *I*(112) | *FWHM* (degree) |
|---|---|---|---|
| Mo/$Al_2O_3$/SS | 470 | 227 | 0.123 |
| Mo/$Al_2O_3$/SS | 530 | 286 | 0.112 |
| Mo/SS | 530 | 406 | 0.109 |

***Optical Reflection***

Figure 4.11 shows the variation of the optical reflectance (*%R*) spectra for the CIGS films deposited at two different temperatures. The interference fringes disappear near the band edge of $\lambda \sim 1000$ nm corresponding to the optical energy gap ($E_g$) of approximately 1.24 eV. The reflectance spectra of the CIGS film on Mo without $Al_2O_3$ barrier shows larger interference oscillations typically seen in the films with high crystal quality which is consistent with the highest intensity of the (112) plane of the CIGS shown in Fig. 4.10 (a). For those films on the Mo with $Al_2O_3$ barrier, the reflection intensity is significantly lower at both high temperature (530°C) and low temperature (470°C). The damping of the oscillations below the gap is possibly due to the differences of refractive index in different layers of film and also defect states in the gap of lower quality CIGS films which directly affect the carriers in the films.

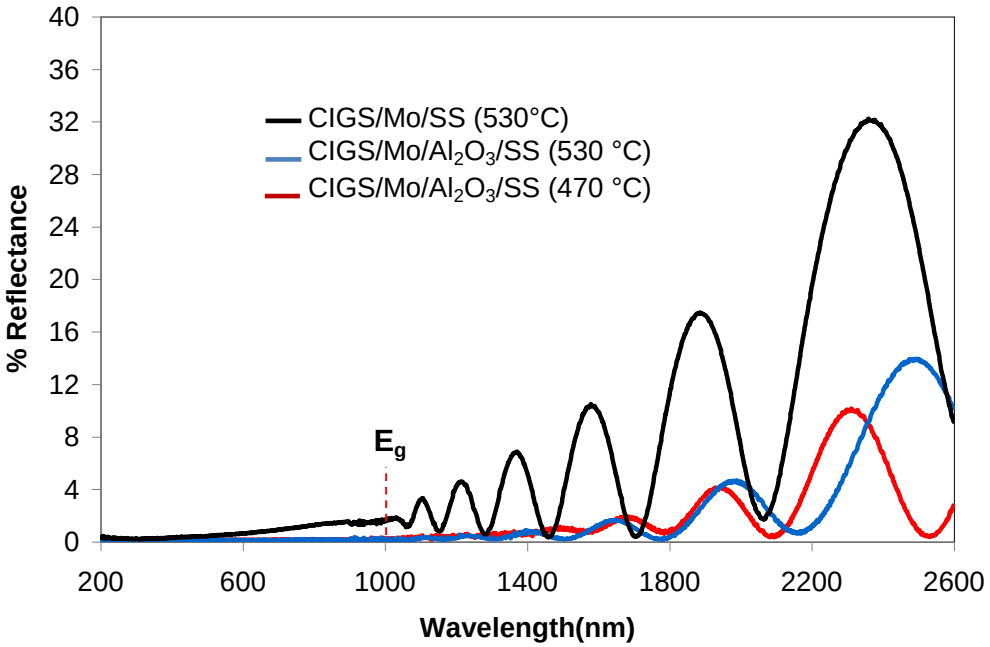


*Figure 4.11: The optical reflectance spectra of CIGS films on Mo/SS at 530°C, Mo/400-nm-$Al_2O_3$/SS at 530°C and Mo/400-nm-$Al_2O_3$/SS at 470°C.*

***Cell performance***

The performances of the CIGS solar cells on the flexible SS substrates are determined from the current-voltage (J-V) measurements. It can be observed that the $Al_2O_3$ barrier directly affects the parameters of the solar cells, e.g. the fill factor (*FF*), the open-circuit voltage ($V_{oc}$) and the short circuit current density ($J_{sc}$). The CIGS on Mo/$Al_2O_3$/SS processed at 530°C has the highest $J_{sc}$ and $V_{oc}$ compared to that processed at 470°C and that on Mo/SS processed at 530°C despite the small grain seen in the CIGS on Mo/$Al_2O_3$/SS. The solar cell parameters are summarized in Table 4.3. The CIGS solar cells grown at lower temperature of 470°C have smaller variations than that at higher temperature.

*Table 4.3: Statistical values of the current-voltage parameters of the solar cells on SS substrates.*

| **Substrate** | $V_{oc}$ (mV) | $J_{sc}$ (mA/cm$^2$) | *FF* (%) | $\eta$ (%) |
|---|---|---|---|---|
| **Mo/$Al_2O_3$/SS (470$^o$C)** | | | | |
| Max | 468 | 26.4 | 46.1 | 5.7 |
| Average | 413 | 25.9 | 39.7 | 4.4 |
| S.D. | 44 | 2.2 | 5.3 | 1.2 |
| **Mo/$Al_2O_3$/SS (530$^o$C)** | | | | |
| Max | 540 | 31.9 | 54.4 | 9.4 |
| Average | 450 | 30.3 | 42.2 | 6.0 |
| S.D. | 102 | 1.9 | 9.0 | 2.5 |
| **Mo/SS (530$^o$C)** | | | | |
| Max | 297 | 8.9 | 33.9 | 0.9 |
| Average | 203 | 7.7 | 29.8 | 0.5 |
| S.D. | 102 | 1.1 | 3.2 | 0.3 |

***Conclusion***

High substrate temperature during the deposition resulting in the large grain of CIGS film and high efficiency compared to those with low substrate temperature. However, the two-stage growth process typically yields lower cell efficiency than the three-stage process which will be discussed in the next section.

## 4.5. Three-stage deposition process for CIGS on flexible SS

### 4.5.1. Three-stage process

This process is started with the deposition of In, Ga and Se or $(In,Ga)_2Se_3$ precursor in the first stage at the low substrate temperature of 400°C and then followed by the deposition of only Cu and Se in the second stage at the higher substrate temperature of 540°C until the overall composition becomes Cu rich ($y$ ~ 1.3). In the third stage, the deposition of In, Ga and Se is allowed with slightly reduction of In and Ga flux from the first stage at high substrate temperature (540°C) until the overall composition is slightly Cu poor ($y$ ~ 0.9) at the end point. The $\frac{[Ga]}{[Ga]+[In]}$ ratio ($x$) is set at 0.37 in order to have $E_g$ ~ 1.3 eV for the CIGS that leads to the increase of p-type doping. The growth process time is about 80 minutes. The growth profile and the film composition of the CIGS in the three stage process are shown in Fig. 4.12.

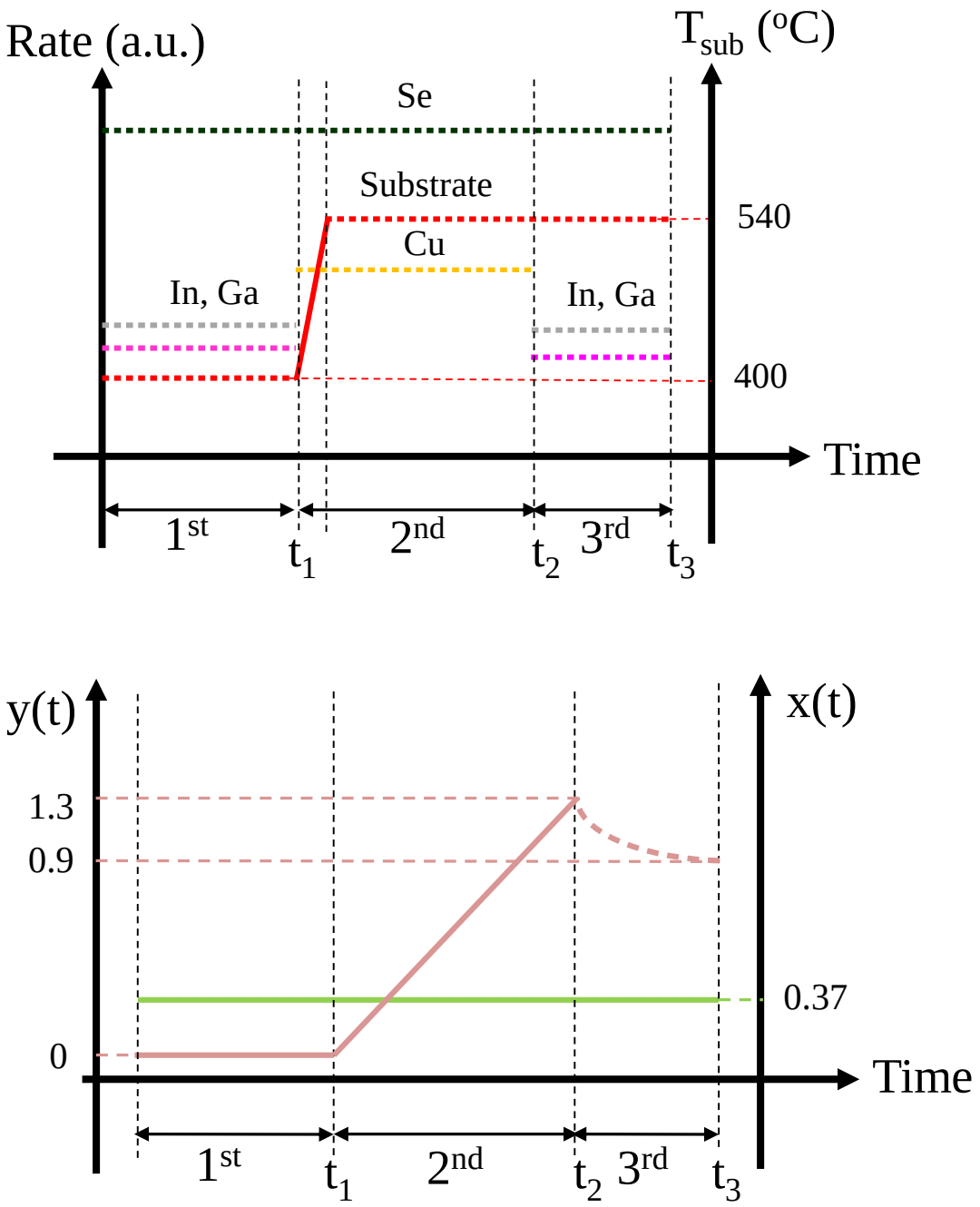


*Figure 4.12: Schematic representations of the growth profile and the film composition for the three stage process.*

The example of the *in-situ* signals of the three-stage process is shown in Fig. 4.13. In the first stage (no Cu flux), the oscillations of the pyrometer signal by the increase of the film thickness appear as observed in the two-stage process. After that, the pyrometer shows higher signal due to the increase of substrate temperature and

also the Cu flux is allowed in the second stage. The composition of the film gradually changes to Cu-rich phase. The end of deposition time in the second stage can be calculated by Eq. (3.7) from stoichiometric composition ($y$=1) that can be observed from the increase of output power signal. In the final stage, the Cu flux is terminated and the film composition changes from the Cu-rich phase to slightly Cu-poor phase at EPD.

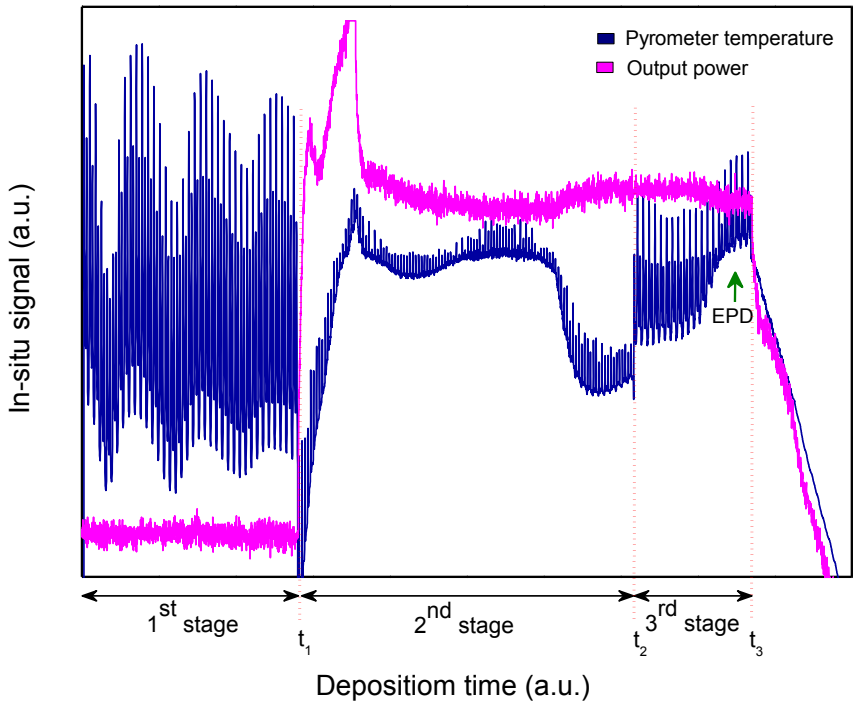


*Figure 4.13: The in-situ monitoring signals for the three-stage process.*

### 4.5.2. $Al_2O_3$ blocking layer or diffusion barrier

Before the deposition of Mo layer, the insulating $Al_2O_3$ thin film is required. The most common form of crystalline α-$Al_2O_3$ is known as corundum which has a trigonal bravais lattice with a space group of R-3c as shown in Fig. 4.14. The corundum structure consists of hexagonal close-packed oxygen atoms with cations filling up two-third of the central octahedral sites.

The important reasons for the selection of $Al_2O_3$ thin film as a blocking layer are:

- Coefficient of thermal expansion (CTE) of $Al_2O_3$ thin film (6-8 $x10^{-6}$/K) is close to that of the SS substrate (10-18 $x10^{-6}$/K depending on types of SS) and the CIGS absorber (7-9 $x10^{-6}$/K); the CTE value has a direct effect to the film adhesion at high temperature during the CIGS deposition,
- Strong ionic interatomic bonding and nanoparticles character; it is an effective blocking layer,
- Chemical inertness; it does not react or corrode with Se atmosphere and CdS solution,
- Good thermal conductivity; the substrate ($Mo/Al_2O_3/SS$) temperature during the CIGS deposition affects the film quality,
- It is an electrical insulator between the metal substrate and the monolithically interconnected solar cell for the flexible solar module.

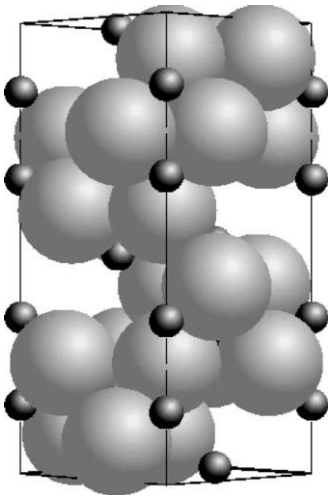

*Figure 4.14: Crystal structure of α-$Al_2O_3$ , the large circle is O atom and the smaller one is Al atom [19].*

$Al_2O_3$ thin film is deposited on the SS substrates by the RF magnetron sputtering technique using the 99.99% pure $Al_2O_3$ ceramic target (4-inch in diameter). During the sputtering, the Argon pressure is kept at $1.8x10^{-3}$ mbar and the RF sputtering power is set at 280 Watt where the substrate holder is fixed. The distance between the substrate holder and the $Al_2O_3$ target is about 6 cm. The deposition rate is about 5-6 nm/min resulting in the high packing density for the blocking of contaminations from the SS substrate into the CIGS absorber layer during the CIGS deposition. The thicknesses of the $Al_2O_3$ layer used in this study are varied from 0 to 2000 nm**.** The experimental results on the fabrication of the $Al_2O_3$ blocking layer are as the followings;

***Surface morphology***

Figure 4.15 shows the surface morphology of the SS substrate covered with the $Al_2O_3$ thin film by the sputtering technique. The AFM image of the $Al_2O_3$ film shows the small grain size of the amorphous $Al_2O_3$ films, thus the diffraction peak of the $Al_2O_3$ films could not be observed by XRD in Fig. 4.10.

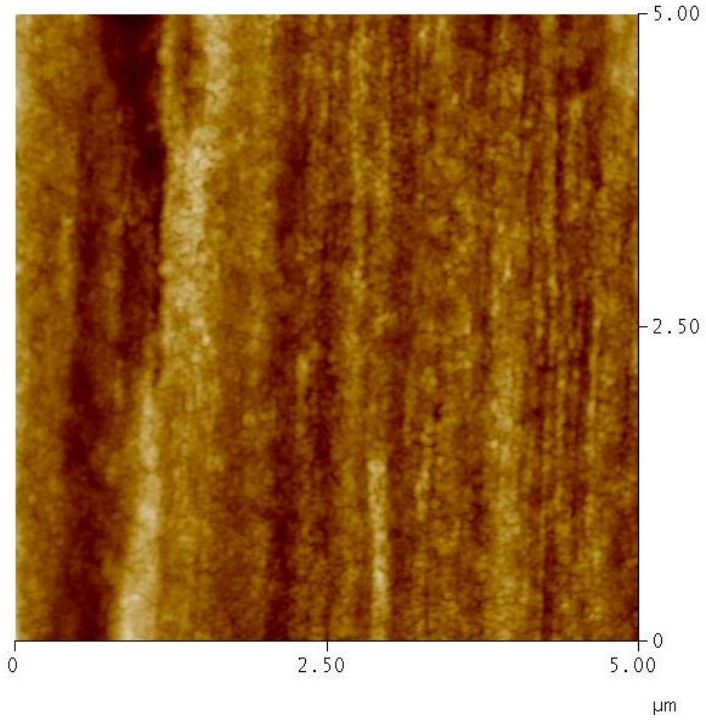


*Figure 4.15: AFM image of $Al_2O_3$ surface deposited on SS substrate.*

***Optical reflection***

The examples of optical reflectance of $Al_2O_3$ films at different thicknesses are shown in Fig. 4.16. Since its energy band gap is quite large ($E_g$ ~ 8 eV) [20], thus the cut-off energy in the range of measurement (200-2000 nm) could not be seen. The intensity of the reflection decreases with the increasing of $Al_2O_3$ thickness due to rough surface of films on SS and the effect of light absorption. The index of refraction of the $Al_2O_3$ film (*n*) is 1.68 [21]. The thickness of the films (*d*) can be determined from the interference fringes of reflection spectra in Eq. (3.12).

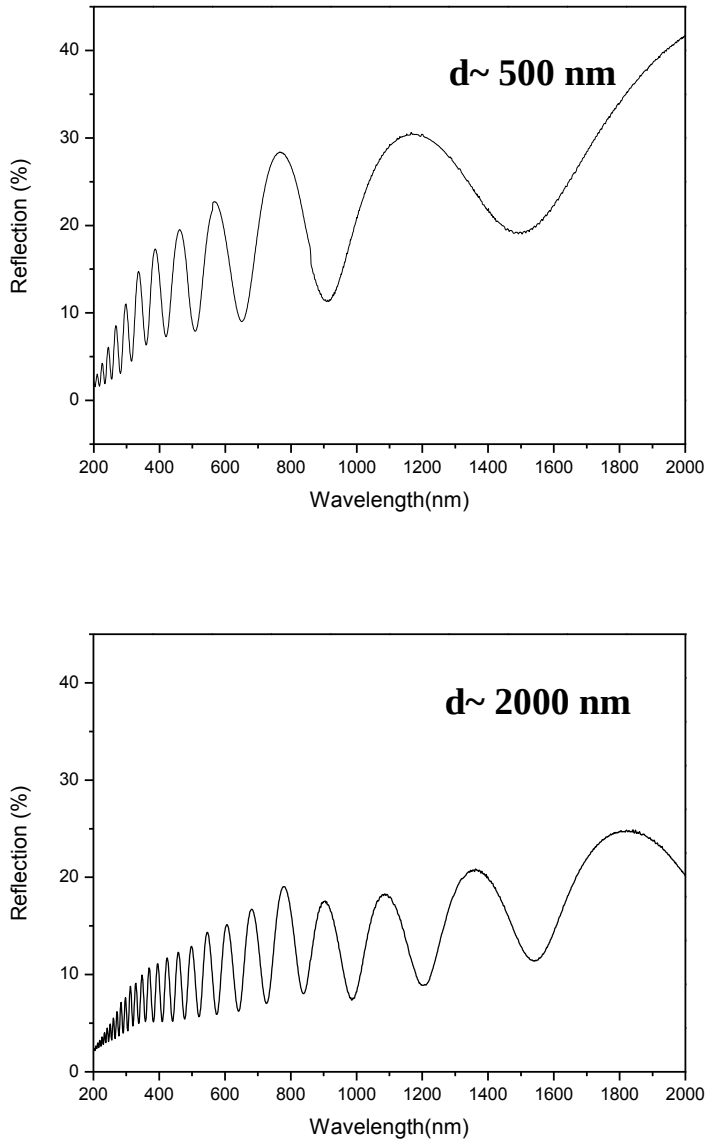


*Figure 4.16: The optical reflection spectra of $Al_2O_3$ films grown on SS substrate at the thickness about 500 and 2000 nm, respectively.*

***Cell parameters***

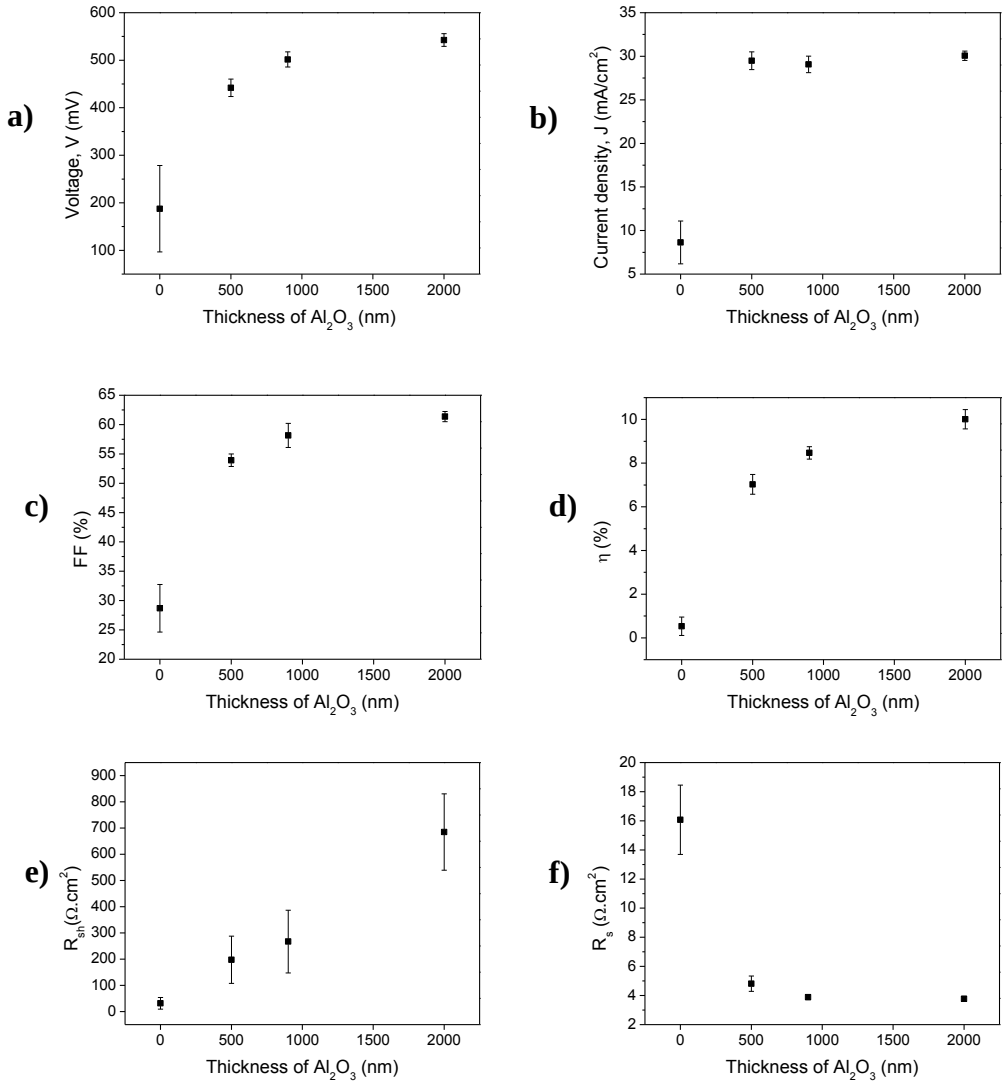


*Figure 4.17: Solar cell parameters (a) $V_{oc}$, (b) $J_{sc}$, (c) FF, (d)$\eta$, (e) $R_{sh}$ and (f) $R_s$ of the flexible CIGS solar cell on SS substrates with different thickness of $Al_2O_3$ blocking layer.*

The results are observed that the thickness of the $Al_2O_3$ barrier directly affects the key parameters of the solar cells, e.g. the open-circuit voltage ($V_{oc}$), the short circuit current ($J_{sc}$), the fill factor ($FF$) and cell efficiency ($\eta$). The $Al_2O_3$ layer effectively reduced the impurity diffusion from the substrate as the increase of the shunt resistances ($R_{sh}$) values of the cells with the thickness of blocking layer caused by the decrease of conducting paths in the CIGS absorber layer from metallic impurities (Fe, Cr and other elements) and internal imperfections of films.

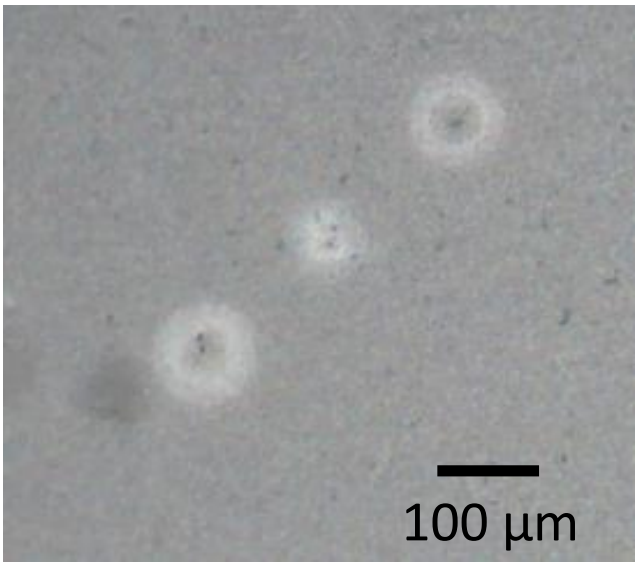


*Figure 4.18: Optical image of CIGS surface showing the diffusion of impurities from the SS substrate.*

On the other hand, the series resistances ($R_s$) values decreased due to the effect of impurity alloying [22] in conducting layers, i.e. front/back contacts and window layer, vanishes as shown in Fig. 4.17 (f) The impurity on the CIGS surface diffused from the lower layers, suspiciously from the SS through the $Al_2O_3$ barrier layer, could be seen in Fig. 4.18.

Moreover, $Al_2O_3$ barrier increases the doping or p-type defects in the CIGS absorber layer and carrier mobility from the reduction of defect states in the gap of CIGS films leading to higher values of $V_{oc}$ and the $J_{sc}$, respectively. The *FF* and $\eta$ of the solar cells on SS substrates with an $Al_2O_3$ barrier are higher than that of the solar cells without a barrier. These parameters in each condition are summarized in Table 4.4. The higher FF indicates the higher CIGS quality for the formation of the p-n junction with the CdS layer when $Al_2O_3$ barrier is used. The highest efficiency obtained is 10.8% on the substrate with 2000 nm thick $Al_2O_3$ barrier. It is worth to note that the parameters of the solar cell obtained here are somewhat lower than that obtained from the standard cells fabricated on the soda-lime glass (SLG) substrate. The J-V curves of the best cells with different thickness of $Al_2O_3$ barrier are summarized in Fig. 4.19.

*Table 4.4: Solar cell parameters from I-V measurement for SS substrates with different thickness of $Al_2O_3$ blocking layer*

| Substrates | $V_{oc}$ (mV) | $J_{sc}$ (mA/cm$^2$) | *FF* (%) | $\eta$ (%) |
|---|---|---|---|---|
| **Mo/SS** | | | | |
| Max | 315 | 10.3 | 34.8 | 1.1 |
| Average | 188 | 8.6 | 28.7 | 0.5 |
| Substrates | $V_{oc}$ (mV) | $J_{sc}$ (mA/cm$^2$) | FF (%) | η (%) |
| **Mo/500 nm-$Al_2O_3$/SS** | | | | |
| Max | 455 | 29.3 | 55.7 | 7.4 |
| Average | 443 | 29.3 | 53.8 | 7.0 |
| **Mo/900 nm-$Al_2O_3$/SS** | | | | |
| Max | 490 | 30.6 | 59.4 | 8.9 |
| Average | 502 | 29.1 | 58.1 | 8.5 |
| **Mo/2000 nm-$Al_2O_3$/SS** | | | | |
| Max | 560 | 30.5 | 62.9 | 10.8 |
| Average | 543 | 30.1 | 61.4 | 10.0 |

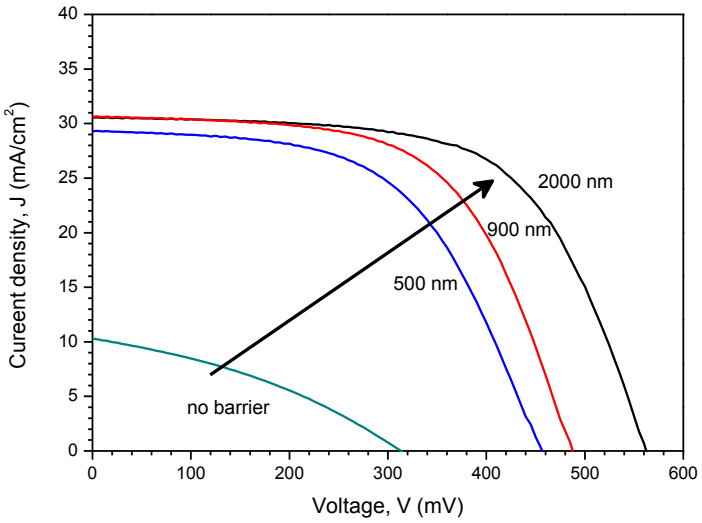


*Figure 4.19: J-V curves of the best cell on SS substrates with different thickness of $Al_2O_3$ blocking layer.*

***Conclusion***

The optimum thickness of $Al_2O_3$ thin film obtained in this work for the blocking of impurity diffusion from SS substrate is about 2000 nm. The highest efficiency is at 10.8%

To improvement the performance of the cell efficiency for flexible substrate, one needs to consider the increasing of doping in the CIGS that could be achieved by the incorporation of Na that is not the native element in the SS substrate.

## 4.6. Na incorporation in CIGS absorber in the three-stage process

One important reason for lower efficiencies of flexible CIGS solar cells on metallic substrates is the lack of natural diffusion of Na into the CIGS absorber layer when compared to the standard CIGS solar cells on soda-lime glass (SLG) or Na containing glass substrates. Sodium (Na) source is well known to help increasing the CIGS solar cell performance. Therefore, an incorporation method for Na is needed for metallic foils or Na free substrates. The benefits of Na incorporation in the CIGS solar cells are:

- Improvement of CIGS morphology and the formation of p-n heterojunction between CIGS and CdS layers, i.e. smoother surface and higher CIGS crystal quality ($R_{sh}$ and $FF$ increase),
- Increasing of hole carrier density and p-type conductivity of the CIGS due to Na substitution at the Cu site ($Na_{Cu}$) at the end point of CIGS growth process; Na can diffuse from the Cu sites to the CIGS surface by the thermal energy causing Cu vacancies that are main acceptor defects in CIGS ($V_{oc}$ and $J_{sc}$ increase),
- Increase solar cell efficiency ($\eta$).

In general, the addition of Na in the CIGS layer can be achieved by various methods:

(1) evaporation of a thin NaF precursor layer before the CIGS deposition,

(2) co-evaporation of a Na compound during the CIGS deposition, and

(3) evaporation after the CIGS deposition and followed by annealing in vacuum, known as Na post-treatment method.

In this work, I choose to have Na enhancement by using the NaF co-evaporation within 7 minutes during the ramping of substrate temperature from low to high temperature in the second stage of three-stage process as shown in Fig. 4.20 (b). From the result of Na precursor on SLG substrate, I have seen that Na is driven to the surface of CIGS in the second stage due to the increase of thermal energy. Higher substrate temperature can increase the Na diffusion into the CIGS layer.

The results of Na enhancement are studied on the cells on the SS substrates without $Al_2O_3$ barrier, substrate with $Al_2O_3$ barrier, and comparison of Na incorporation at different steps of CIGS deposition; NaF precursor, NaF co-evaporation in the second stage and the third stage.

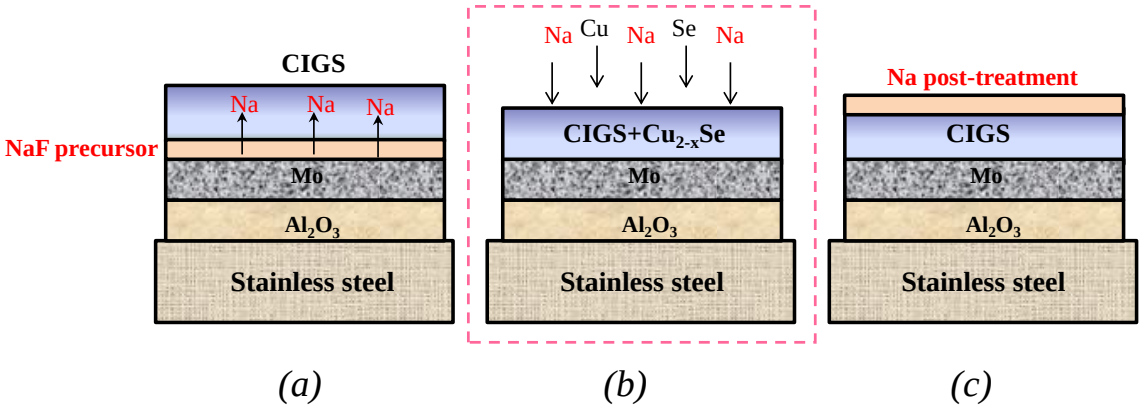


*Figure 4.20: Na incorporation methods for the flexible solar cells: (a) NaF precursor layer [23] (b) NaF co-evaporation [24]and (c) Na post-treatment [25].*

### 4.6.1. Na effect on the Mo/SS substrate

This section describes the Na incorporation using the Mo/SS substrate with the NaF equivalent of 100 Å thick.

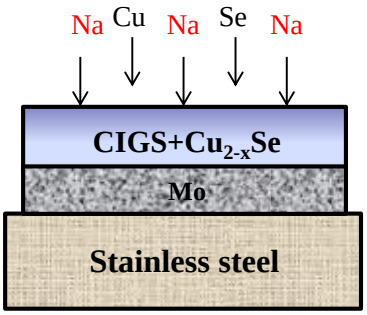


*Figure 4.21: Schematic diagram of the Na incorporation during the CIGS growth on the SS substrate without $Al_2O_3$ blocking layer*

*Table 4.5: Solar cell parameters on SS substrates without $Al_2O_3$ barrier by using NaF incorporation in the second stage*

| NaF thickness | $V_{oc}$ (mV) | $J_{sc}$ (mA/cm$^2$) | $FF$ (%) | $\eta$ (%) |
|---|---|---|---|---|
| **No NaF ( Mo/SS)** | | | | |
| Max | 315 | 10.3 | 34.8 | 1.1 |
| Average | 188 | 8.6 | 28.7 | 0.5 |
| **100 Å-NaF (Mo/SS)** | | | | |
| Max | 475 | 5.8 | 40.1 | 1.1 |
| Average | 444 | 4.6 | 39.3 | 0.8 |

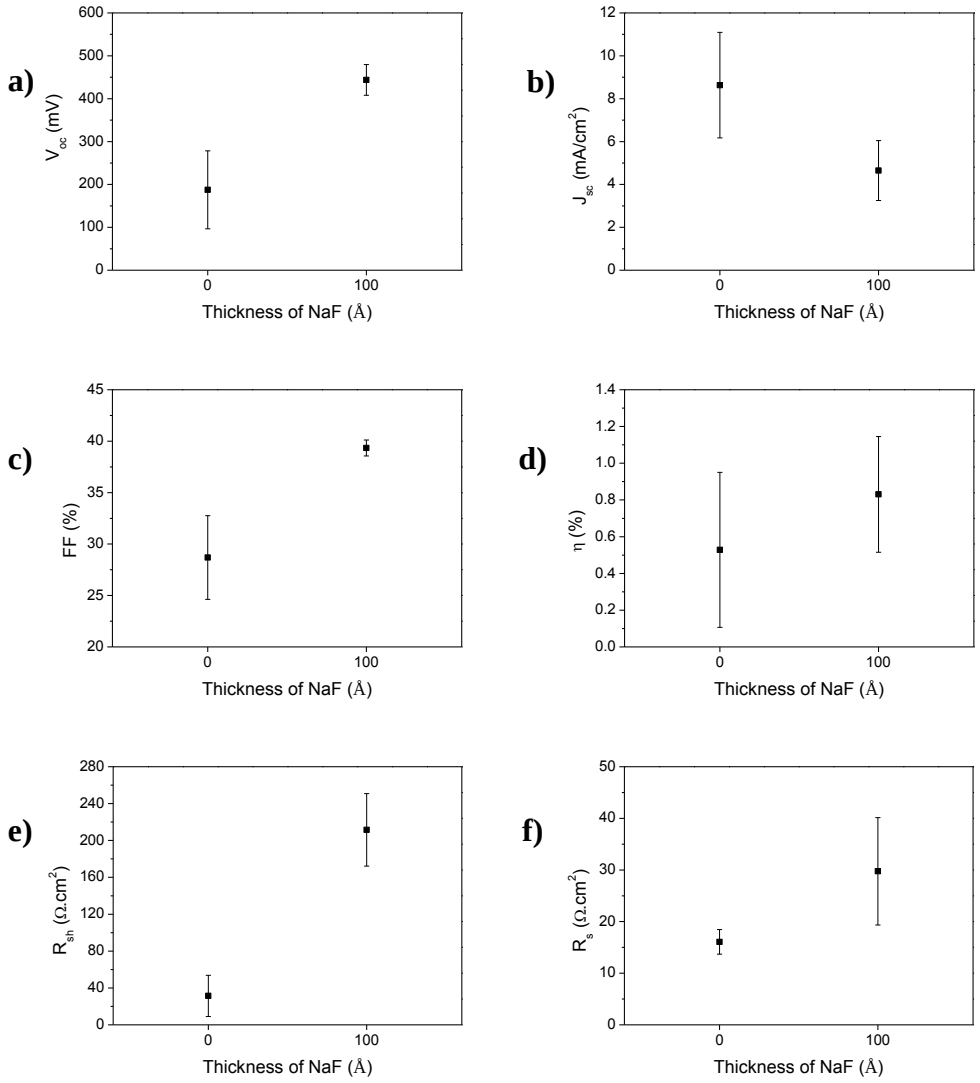


*Figure 4.22: Solar cell parameters on Mo/SS substrates with and without Na*

Table 4.5 and Fig. 4.22 summarize the effect of Na to the performance of the flexible CIGS solar cells without $Al_2O_3$ barrier. It can be seen that the addition of Na results in the enhancement of $V_{oc}$, $FF$ and $R_{sh}$. However, these parameters are still lower than those of the cells with $Al_2O_3$ blocking layer. Na increases the p-type doping and uniformity of CIGS film that is observed from smoother CIGS surface leading to a good p-n junction formation. On the other hand, $J_{sc}$ decrease with the increasing of $R_s$ caused by alloying effect in the CIGS and the metal contact layers. However, the addition of Na does not have a significant effect to the efficiency on the cells without $Al_2O_3$ blocking layer due to the diffusion of impurities.

### 4.6.2. Na effect on Mo/$Al_2O_3$/SS substrate

It has been shown that the $Al_2O_3$ blocking layer is necessary to prevent or reduce the diffusion of impurities, in this section, the relationship between the thickness of NaF and the cell parameters on the Mo/2000 nm-$Al_2O_3$/SS substrate will be described. The equivalent thicknesses of NaF used in this work are in the range of 30-200 Å.

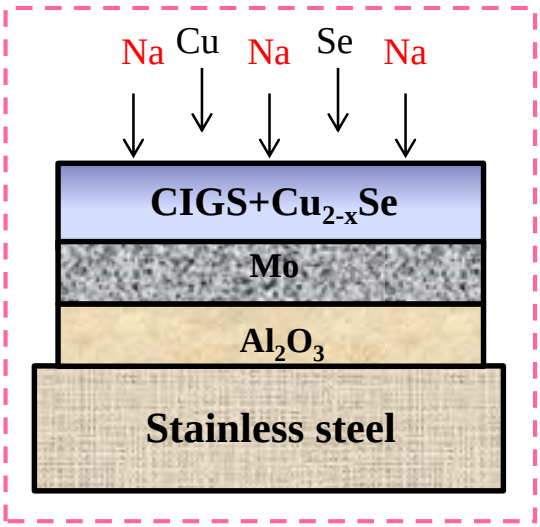


*Figure 4.23: Schematic diagram of the Na incorporation during the CIGS growth on the SS substrate with 2000 nm thick $Al_2O_3$ blocking layer*

*Table 4.6: Solar cell parameters on SS substrates with 2000 nm thick-$Al_2O_3$ barrier with different thicknesses of NaF*

| NaF thickness | $V_{oc}$ (mV) | $J_{sc}$ (mA/cm$^2$) | *FF* (%) | $\eta$ (%) |
|---|---|---|---|---|
| **No NaF (Mo/2000 nm-$Al_2O_3$/SS)** | | | | |
| Max | 560 | 30.5 | 62.9 | 10.8 |
| Average | 543 | 30.1 | 61.4 | 10.0 |
| **30 Å-NaF ( Mo/2000 nm-$Al_2O_3$/SS)** | | | | |
| Max | 640 | 30.7 | 72.1 | 14.2 |
| Average | 636 | 29.7 | 71.9 | 13.6 |
| **50 Å-NaF ( Mo/2000 nm-$Al_2O_3$/SS)** | | | | |
| Max | 630 | 32.9 | 73.9 | 15.3 |
| Average | 626 | 31.4 | 73.7 | 14.5 |
| **80 Å-NaF ( Mo/2000 nm-$Al_2O_3$/SS)** | | | | |
| Max | 635 | 31.3 | 71.7 | 14.2 |
| Average | 629 | 29.9 | 71.9 | 13.5 |
| **100 Å-NaF ( Mo/2000 nm-$Al_2O_3$/SS)** | | | | |
| Max | 645 | 31.1 | 70.3 | 14.1 |
| Average | 641 | 30.3 | 70.7 | 13.7 |
| **120 Å-NaF ( Mo/2000 nm-$Al_2O_3$/SS)** | | | | |
| Max | 640 | 31.2 | 70.6 | 14.1 |
| Average | 634 | 30.2 | 69.2 | 13.3 |
| **150 Å-NaF ( Mo/2000 nm-$Al_2O_3$/SS)** | | | | |
| Max | 600 | 22.4 | 60.5 | 8.1 |
| Average | 590 | 22.0 | 60.7 | 7.9 |
| **200 Å-NaF (Mo/2000 nm-$Al_2O_3$/SS)** | | | | |
| Max | 560 | 20.6 | 59.0 | 6.8 |
| Average | 548 | 20.2 | 55.9 | 6.2 |

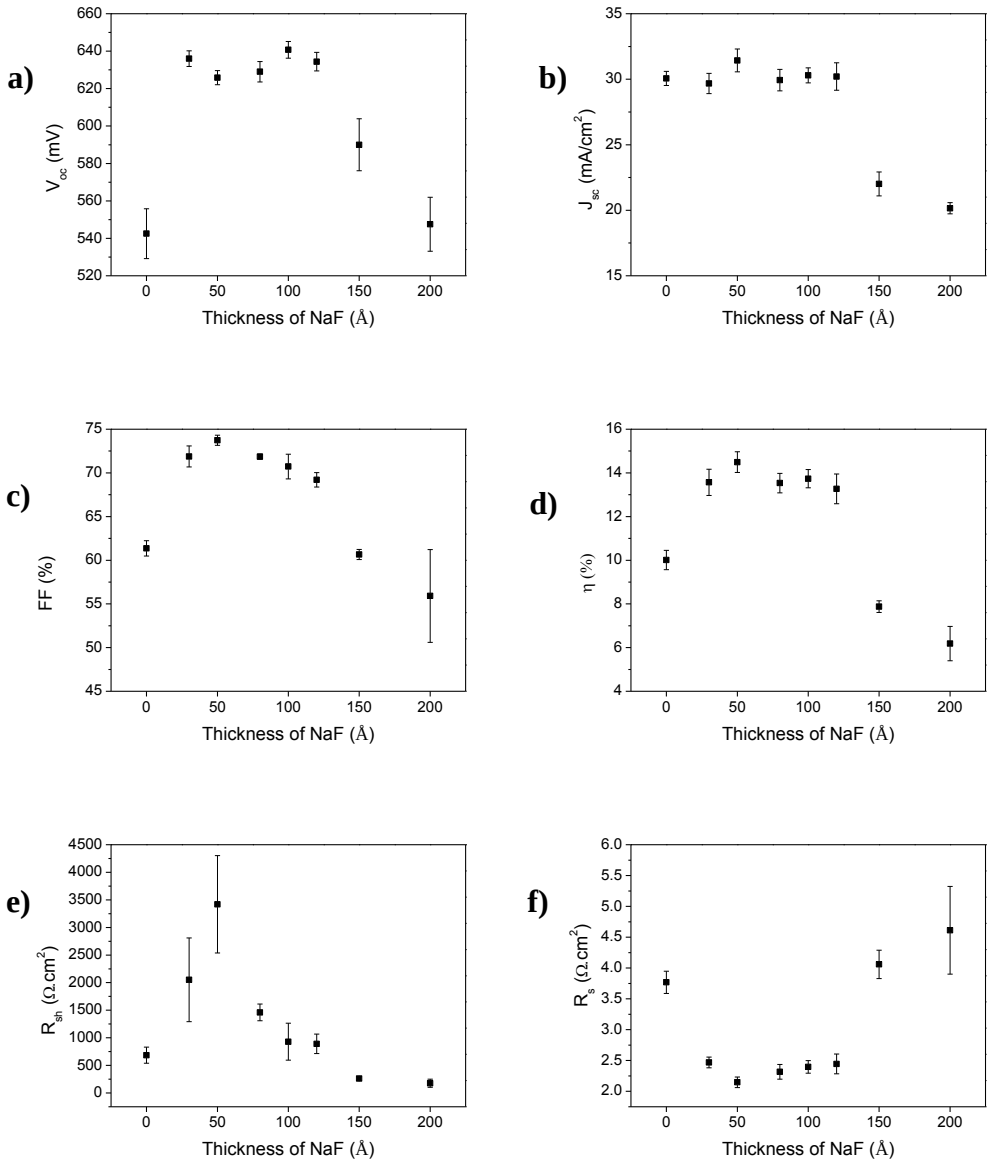


*Figure 4.24: Solar cell parameters on Mo/2000 nm-$Al_2O_3$/SS substrates with different NaF thicknesses*

The results show that the increase of $V_{oc}$ and *FF* with NaF thickness. However, when excessive NaF is used the $V_{oc}$ and *FF* decrease due to residual Na in the CIGS layer resulting in the decreasing of doping and the quality of junction formation. At the equivalent of 100 Å thick of NaF the maximum $V_{oc}$ or high doping in the CIGS layer is obtained, but at 50 Å thick NaF yields the maximum *FF* or high CIGS quality for the junction formation with CdS buffer layer that consistent with the highest $R_{sh}$ values shown in Fig. 4.24 (e). The effect of Na to the $J_{sc}$ of solar cell is similar when

the thickness of NaF is in the range of 30-120 Å while the current rapidly decreases, and also the increasing of $R_s$ values when the thickness of NaF is higher than 120 Å. The latter is due to the small grain size of CIGS that could lead to high carrier recombination rate, as shown by the corresponding to SEM image in Fig. 4.25 (a). The highest efficiency obtained in this work is 15.3% from the CIGS films with equivalent of 50 Å thick NaF on the Mo/2000 nm thick $Al_2O_3$/SS substrate.

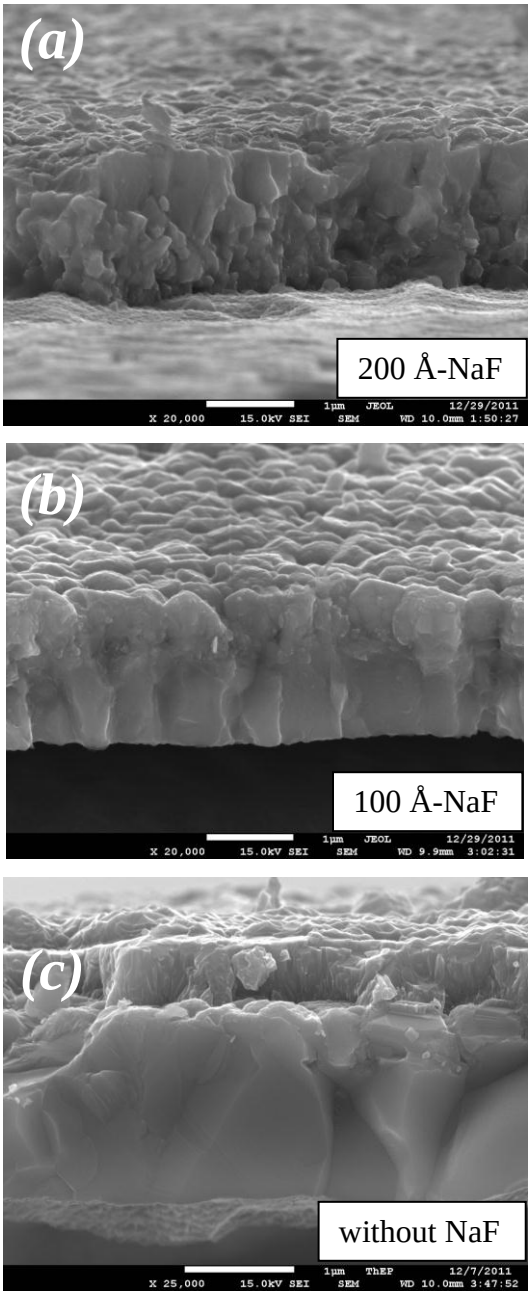


*Figure 4.25: SEM cross-section images of the CIGS films on the 2000 nm-$Al_2O_3$/SS substrates (a) with 200 Å-NaF and (b)with 100 Å-NaF and (c) without NaF.*

### 4.6.3. Comparison of CIGS solar cells using different step of Na incorporation

The NaF precursor and NaF co-evaporation in the third stage are also prepared in order to compare with the results of NaF co-evaporation in the second stage by using the same thickness of NaF at 50 Å. The results summarized in Table 4.6 show that $V_{oc}$ increases for the cells with NaF precursor and co-evaporation in the third stage methods, but the $J_{sc}$ values decrease when compared with co-evaporation in the second stage.

***Conclusion***

The steps of Na incorporation in the CIGS growth process result in small change of efficiency. The most important thing is the content of incorporated Na. The optimum of NaF equivalent thickness is approximately 50 Å to achieve the highest efficiency by co-evaporation method in the second stage. The J-V characteristics between the best flexible CIGS solar cell by NaF co-evaporation in the second stage and the standard CIGS cell on SLG substrate with the efficiency of 16% are compared and shown in Fig. 4.26.

*Table 4.7: Parameters of solar cells grown with different step of Na incorporation (NaF =50Å)*

| Cell parameters | NaF precursor | NaF co-evaporation in | |
|---|---|---|---|
| | | $2^{nd}$ stage | $3^{rd}$ stage |
| $V_{oc}$ (mV) | 646 | 626 | 651 |
| $J_{sc}$ (mA/cm$^2$) | 28.1 | 31.4 | 27.8 |
| *FF* (%) | 74.5 | 73.7 | 73.8 |
| $\eta$ (%) | 13.5 | 14.5 | 13.3 |

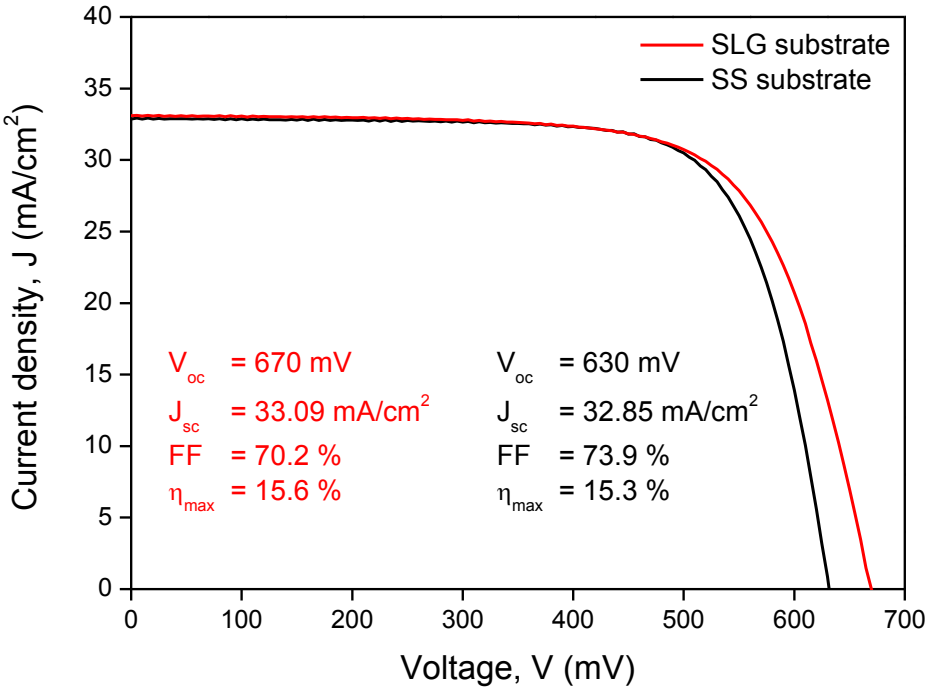


*Figure 4.26: J-V curves of the best CIGS cell on SS substrate (black line) with 2000 nm thick-$Al_2O_3$ and 50 Å thick-NaF compared with the best CIGS cell on SLG*

# Chapter V

## Summary Remarks

In this thesis, I have successfully fabricated the high efficiency flexible CIGS thin film solar cells on the ferritic stainless steel (SS) substrates (type 430). To achieve that, $Al_2O_3$ as the impurity blocking layer thickness, substrate temperature during the CIGS processing and the Na incorporation techniques have been implemented. The effects from these factors can be summarized as followed;

- Effect of diffusion barrier and substrate temperature

The $Al_2O_3$ barrier layer is necessary for the CIGS solar cells on flexible SS substrates in order to prevent or reduce the diffusion of the metallic impurities (Fe, Cr, etc.) from the SS substrate through the Mo back-contact into the CIGS absorber layer. Higher substrate temperature ($T > 500^oC$) has an impact on the quality of the devices despite the higher rates of impurities diffused into the growing CIGS layer. However, at low substrate temperature, the quality of the CIGS devices is not as good as ones processed at higher temperature. Thus the substrate temperature is one important factor to the growth of CIGS in order to compete between the diffusion of impurities and the intrinsic properties of the CIGS absorber such as grain size, p-type doping, etc. The performance of the CIGS solar cells on the SS substrate increases with the thickness of the $Al_2O_3$ barrier. The working thickness of blocking layer for the best cell ($\eta$~10.8% without Na) is approximately 2000 nm from the CIGS films fabricated by the three-stage process at the highest temperature of about $540^oC$ during the deposition.

- Effect of Na enhancement

The quality of the p-n junction formation and p-type doping in the CIGS layer is directly related with the Na content. The NaF compound is chosen as an external Na source in this work. The NaF is co-evaporated during the ramping up of the

substrate temperature such that Na can diffuse and mix with CIGS and $Cu_{2-x}Se$ liquid phase in the second stage. Appropriate amount of Na can enhance the key parameters of the solar cell such as $V_{oc}$ and *FF*. In contrast, too high Na content (>120 Å) results in the decrease of $V_{oc}$, *FF* and $J_{sc}$ due to the residual Na. The optimum equivalent thickness of NaF for flexible SS substrate is about 50 Å to obtain the highest efficiency of flexible CIGS solar cell of about 15.3% which is comparable to that of the CIGS solar cell on SLG substrate. In addition, Na plays the important role to suppress the diffusion of Ga resulting in double Ga-graded phenomena in the CIGS layer. This effect produces the back surface field that raises the carrier collection at the metal grid.

The suggestion of this work for flexible CIGS thin film solar cells on SS substrates are:

- Study the Ga-graded in the CIGS layer for Na enhancement at different steps of CIGS deposition in order to improve the CIGS growth process,
- Change the Na source from unstable NaF compound to stable Na compound such as alkali silicate or SLG thin film that is non-toxic material.

# References


[1] Karsten Otte, Liudmila Makhova, Alexander Braun and Igor Konovalov**.** Flexible Cu(In,Ga)$Se_2$ thin-film solar cells for space application. *Thin Solid Films* 511 – 512 (2006): 613 – 622**.**

[2] Friedrich Kessler and Dominik Rudmann. Technological aspects of flexible CIGS solar cells and modules. *Solar Energy* 77 (2004): 685–695.

[3] F. Kessler, D. Herrmann and M. Powalla. Approaches to flexible CIGS thin-film solar cells. *Thin Solid Films* 480–481 (2005): 491– 498.

[4] A. Stuke, H. Behrens, B.C. Schmidt and R. Dupree. $H_2O$ Speciation in float Glass and Sods Line Silica Glass. *Chem. Geol.* 229 (2006): 64-77.

[5] E. Jaffe and A. Zunger. Theory of the Band-Gap Anomaly in $ABC_2$ chalcopyrite Semiconductor. *Phys. Rev.B* 29 (1984): 1882-1906.

[6] S.H. Wei, S.B. Zhang and A. Zunger. A.Effects of Ga addition to $CuInSe_2$ on its electronic, structure and defect properties. *Appl. Phys. Lett.* 72 (1998): 3199-3201.

[7] J.H. Moller. Semiconductor for Solar Cells. Boston, London: *Artech House* (1993): 1-49.

[8] R. Sakdanuphab. *Influence of sodium in fabrication process of high efficiency CIGS thin film solar cells*. Ph.D. thesis, Department of Physics Faculty of Science Chulalongkorn University, 2010.

[9] Vegard, L. Die Konstitution der Mischkristalle und die Raumfüllung der Atome. Zeitschrift für Physik, 5:17, 1921.

[10] C.H. Chang, A. Davydov, B.J. Stanbery and T.J. Anderson. Thermodynamic Assessment of the Cu-In-Se System and Application to Thin Film Photovoltaics. *Proc. 25$^{th}$ PVSC.* (1996): 849-852.

[11] R. H. Bube. Photovoltaic Material, London: *Imperial College Press*, 1998.

[12] C. H. P. Lupis. Chemical Thermodynamics of Materials**.** North-Holland, Amsterdam (1983).

[13] Y.S. Touloukian, R.K. Kirby, R.E. Taylor and T.Y.R. Lee. Thermophysical Properties of Matter: Thermal Expansion 13, New York: *IFI/Plenum Press*, 1977.

[14] C.A. Kaufmann, A. Neisser, R. Klenk and R. Scheer. Transfer of Cu(In,Ga)$Se_2$ thin film solar cells to flexible substrates using an in situ process control. *Thin Solid Films* 480–481 (2005): 515– 519.

[15] A. M. Gabor, J. R. Tuttle, D. S. Albin, M. A. Contreras, R. Noufi, and A. M. Hermann. High-Efficiency $CuIn_xGa_{1-x}Se_2$ Solar-Cells Made from $(In_x,Ga_{(1-x)})_2Se_3$ Precursor Films. *Appl. Phys.Lett.* 65 (1994): 198–200.

[16] R. Ortega-Borges and D. Lincot. Mechanism of Chemical Bath Deposition of Cadmium Sulfide Thin Films in the Ammonia-Thiourea System. *J. Electrochem. Soc.* 140 (1993): 3464–3473.

[17] J. Ralston, I. Larson, W. Rutland and A. Adam. Feiler. Atomic Force Microscopy and Direct Surface Force Measurements. *Pure Appl. Chem.* 77, 12 (2005): 2149–2170.

[18] Product Data Sheet (Stainless Steel 301, 316L and 430) from AK Steel Corporation

[19] G. Pari, A. Mookerjeee and A.K. Bhattacharya. Study of α-$Al_2O_3$ and the role of Y in $YAlO_3$ and $Y_3Al_5O_{12}$ by first principles electronic structure calculations. *Physica B* 353 (2004): 192–200.

[20] J. Toofan and P.R. Watson. The termination of the α -$Al_2O_3$ (0001) surface: a LEED crystallography determination. *Surface Science* 401 (1998): 162–172.

[21] Chang-Wook Jeong, Jang-Sik Lee ang Seung-Ki Joo. Plasma-Assisted Atomic Layer Growth of High-Quality Aluminum Oxid Thin Films. *Jpn. J. Appl. Phys* (2001).

[22] K.Herz, F.Kessler, R.Wa¨chter, M.Powalla, J.Schneider, A.Schulz, and U.Schumacher. Dielectric barriers for flexible CIGS solar modules. *Thin Solid Films* 403 –404 (2002): 384–389.

[23] M. Bodegard, K. Granath, and L. Stolt. Growth of Cu(In,Ga)Se2 thin films by coevaporation using alkaline precursors. *Thin Solid Films* 361-362 (2000): 9–16.

[24] M. Lammer, U. Klemm, and M. Powalla. Sodium Co-Evaporation for Low Temperature Cu(In,Ga)$Se_2$ Deposition. *Thin Solid Films* 387 (2001): 33–36.

[25] D. Rudmann, M. Kaelin, F.-J. Haug, F. Kurdesau, H. Zogg, A.N. Tiwari, Proc. of the 3$^{rd}$World Conf. on Photovolt. Energy Conversion, Osaka, (2003): 376.

# APPENDICES

# APPENDIX A

## List of Symbols and Abbreviations

| | |
|---|---|
| AFM | Atomic force microscopy |
| AM 1.5, AM 0 | Air mass 1.5, air mass 0 |
| CBD | Chemical bath deposition |
| CGS | Copper gallium diselenide |
| CIGS | Copper indium gallium diselenide |
| CIS | Copper indium diselenide |
| DC | Direct current |
| $E_C$ | Conduction band energy |
| $E_F$ | Fermi energy |
| $E_g$ | Energy band gap |
| $E_V$ | Valance band energy |
| EDS | Energy dispersive X-ray spectroscopy |
| EPD | End point detection |
| FF | Fill factor |
| FESEM | Field emission scanning electron microscope |
| I-V | Current-Voltage |
| $J_0$ | Saturation current density |

| | |
|---|---|
| $J_{sc}$ | Short-circuit current density |
| k | Boltzmann constant |
| MBD | Molecular beam deposition |
| NREL | National Renewable Energy Laboratory |
| NIR | Near infrared |
| PVD | Physical vapor deposition |
| QCM | Quartz crystal thickness monitor |
| %R | Optical refraction |
| RF | Radio frequency |
| $R_s$ | Series resistance |
| $R_{sh}$ | Shunt resistance |
| SEM | Scanning electron microscope |
| SIMS | Secondary ion mass spectroscopy |
| SLG | Soda-lime glass |
| SS | Stainless steel |
| TCO | Transparent conducting oxide |
| $T_{sub}$ | Substrate temperature |
| $T_{pyro}$ | Pyrometer temperature |
| UV | Ultra violet |
| VIS | Visible |
| $V_{oc}$ | Open-circuit voltage |

| | |
|---|---|
| x | [Ga]/([In]+[Ga]) ratio |
| XRD | X-ray diffraction |
| y | [Cu]/([In]+[Ga]) ratio |

# APPENDIX B

## Stainless Steel Data Sheet

### Type 301

Type 301 is an austenitic chromium-nickel stainless steel that provides high strength and good ductility when cold worked. It is a modification of Type 302 in which the chromium and nickel contents are lowered to increase the cold work-hardening range. This permits higher tensile strengths to be achieved by rolling with a lower loss of ductility than with Type 302.

The grade is essentially non-magnetic when annealed. However, when the grade is cold worked, it becomes slightly more magnetic than other standard austenitic stainless steels.

High strength and excellent corrosion resistance make Type 301 Stainless Steel useful for a wide variety of applications. Typical uses include aircraft structural parts, trailer bodies, diaphragms, utensils, architectural and automotive trim, automobile wheel covers, roof drainage products, table-wear, storm door frames and conveyor belts.

| COMPOSITION | % |
|---|---|
| Manganese | 2.00 max. |
| Sulfur | 0.030 max. |
| Chromium | 16.00 - 18.00 |
| Carbon | 0.15 max. |
| Phosphorus | 0.045 max. |
| Silicon | 0.75 max. |
| Nickel | 6.00 - 8.00 |
| Nitrogen | 0.10 max. |
| Iron | Balance |

**PHYSICAL PROPERTIES**

| **Density** | 7.88 g/cm$^3$ |
|---|---|
| **Electrical Resistivity (20°C)** | 69.5 μΩ-cm |
| **Specific Heat (0-100°C)** | 0.50 kJ/kg.K |
| **Thermal Conductivity** | **W/m.K** |
| at 100°C | 16.2 |
| at 500°C | 21.4 |
| **Mean Coefficient of Thermal Expansion** | **μm/m.K** |
| 0 - 100°C | 16.9 x 10$^{-6}$ |
| 0 - 315°C | 17.8 x 10$^{-6}$ |
| 0 - 538°C | 18.4 x 10$^{-6}$ |
| 0 - 649°C | 18.7 x 10$^{-6}$ |
| **Modulus of Elasticity** | **MPa** |
| in tension | 193 x 10$^3$ |
| in torsion | 78 x 10$^3$ |
| **Melting Range** | 1399 - 1421°C |

## Type 316

Type 316 is an austenitic chromium-nickel stainless steel containing molybdenum. This addition increases general corrosion resistance, improves resistance to pitting from chloride ion solutions, and provides increased strength at elevated temperatures. Properties are similar to those of Type 304 except that this alloy is somewhat stronger at elevated temperatures. Corrosion resistance is improved, particularly against sulfuric, hydrochloric, acetic, formic and tartaric acids; acid sulfates and alkaline chlorides. Type 316L is an extra-low carbon version of Type 316 that minimizes harmful carbide precipitation due to welding. Typical uses include exhaust manifolds, furnace parts, heat exchangers, jet engine parts, pharmaceutical and photographic equipment, valve and pump trim, chemical equipment, digesters, tanks, evaporators, pulp, paper and textile processing equipment, parts exposed to marine atmospheres and tubing. Type 316L is used

extensively for weldments where its immunity to carbide precipitation due to welding assures optimum corrosion resistance.

| COMPOSITION | Type 316 (%) | Type 316L (%) |
|---|---|---|
| Phosphorus | 0.045 max. | 0.045 max. |
| Chromium | 16.00 - 18.00 | 16.00 - 18.00 |
| Carbon | 0.08 max. | 0.03 max. |
| Sulfur | 0.030 max. | 0.03 max. |
| Manganese | 2.00 max. | 2.00 max. |
| Silicon | 0.75 max. | 0.75 max. |
| Nickel | 10.00-14.00 | 10.00-14.00 |
| Molybdenum | 2.00 - 3.00 | 2.00 - 3.00 |
| Nitrogen | 0.10 max. | 0.10 max. |
| Iron | Balance | Balance |

**PHYSICAL PROPERTIES**

| | |
|---|---|
| **Density** | 7.99 g/cm3 |
| **Electrical Resistivity (20°C)** | 74 μΩ-cm |
| **Specific Heat (0-100°C)** | 0.50 kJ/kg.K |
| **Thermal Conductivity** | **W/m.K** |
| at 100°C | 16.2 |
| at 500°C | 21.4 |
| **Mean Coefficient of Thermal Expansion** | **μm/m.K** |
| 0 - 100°C | $16.0 \times 10^{-6}$ |
| 0 - 315°C | $16.2 \times 10^{-6}$ |
| 0 - 538°C | $17.5 \times 10^{-6}$ |
| 0 - 649°C | $18.5 \times 10^{-6}$ |
| 0 - 871°C | $19.9 \times 10^{-6}$ |
| **Modulus of Elasticity** | **MPa** |
| in tension | $193 \times 10^{3}$ |
| in torsion | $77 \times 10^{3}$ |
| **Melting Range** | 1371 - 1399°C |

## Type 430

Type 430 is one of the most widely used of the "non-hardenable" ferritic stainless steels. It combines good corrosion resistance and heat and oxidation resistance up to 1500°F (816°C) with good mechanical properties. Typical consumer product applications include automotive trim and molding, furnace combustion chambers, dishwashers, range hoods, gas burners on heating units, gutters and downspouts, steam iron bases and flatware. Industrial and commercial applications range from interior architectural applications to nitric acid plant equipment, oil refinery equipment, roofing and siding and restaurant equipment.

| **COMPOSITION** | **%** |
|---|---|
| Manganese | 1.00 max. |
| Sulfur | 0.030 max. |
| Carbon | 0.12 max. |
| Phosphorus | 0.040 max. |
| Silicon | 1.00 max. |
| Chromium | 16.0-18.0 |
| Nickel | 0.50 max. |
| Iron | Balance |

**PHYSICAL PROPERTIES**

| | |
|---|---|
| **Density** | 7.74 g/cm$^3$ |
| **Electrical Resistivity (21°C)** | 60 μΩ-cm |
| **Specific Heat (0-100°C)** | 0.46 kJ/kg.K |
| **Thermal Conductivity** | **W/m.K** |
| at 100°C | 26.1 |
| at 500°C | 26.3 |
| **Coefficient of Thermal Expansion** | **μm/m.K** |
| 0 - 100°C | 10.4 x 10$^{-6}$ |
| 0 - 538°C | 11.4 x 10$^{-6}$ |
| **Modulus of Elasticity** | 200 x 10$^3$ MPa |

# APPENDIX C

## List of Publications

1. W. Thongkham, R. Sakdanuphab, C. Chityuttakan and S. Chatraphorn, "Influence of $Al_2O_3$ barrier to the efficiency of Cu(In,Ga)$Se_2$ thin film solar cells on flexible stainless steel foils" *Thai Jounal of Physics* Series 6 (2010).
2. W. Thongkham, R. Sakdanuphab, C. Chityuttakan and S. Chatraphorn "Effect of diffusion barrier and substrate temperature to physical properties of flexible Cu(In,Ga)$Se_2$ thin film solar cells" *Journal of Metals, Materials and Minerals* Vol.20 No.3 (2010): 61-65.

# VITAE

Warittha Thongkham was born on 10th July 1985 in Nakhon Sri Thammarat province, Thailand. She received the Bachelor degree of Science (Second Class Honors) in Electronic Physics from Thammasat University in 2008.

## Conference Presentations:

### Poster Presentation

2010 W. Thongkham, R. Sakdanuphab, C. Chityuttakan and S. Chatraphorn., "Influence of $Al_2O_3$ Barrier to the Efficiency of Cu(In,Ga)$Se_2$Thin Film Solar Cells on Flexible Stainless Steel Foils", Siam Physics Congress 2010, River Kwai Village Hotel, Kanchanaburi, Thailand, March 25-27, (2010)

2010 W. Thongkham, R. Sakdanuphab, C. Chityuttakan and S. Chatraphorn., "Flexible Cu(In,Ga)$Se_2$ Thin Films Solar Cells: Roles of $Al_2O_3$ Diffusion Barrier and Substrate Temperature", The 6th Mathematics and Physical Science Graduate Congress 2010 (6th MPSGC), University of Malaya, Malaysia, December 13-15, (2010)

### Oral Presentation

2010 W. Thongkham, R. Sakdanuphab, C. Chityuttakan and S. Chatraphorn., "Effect of Diffusion Barrier and Substrate Temperature to the Physical Properties of Flexible Cu(In,Ga)$Se_2$Thin Film Solar Cells", The Sixth Thailand Materials Science and Technology Conference (MSAT-6), Miracle Grand Convention Hotel, Thailand, August 26-27, (2010)